Agricultural and Forest Meteorology 372 (2025) 110621

Contents lists available at ScienceDirect

Agricultural and Forest Meteorology

journal homepage: www.elsevier.com/locate/agrformet

Daytime water and CO_2 exchange within and above the Amazon rainforest

Raquel González-Armas [a,*], Daniël Rikkers [a], Oscar Hartogensis [a], Cléo Quaresma Dias-Júnior [e], Shujiro Komiya [d], Giovanni Pugliese [b], Jonathan Williams [b,f], Hella van Asperen [d], Jordi Vilà-Guerau de Arellano [a,b], Hugo J. de Boer [c]

[a] Meteorology and Air Quality Section, Wageningen University and Research, 6708 PB, Wageningen, The Netherlands
[b] Atmospheric Chemistry Department, Max Planck Institute for Chemistry, 55128, Mainz, Germany
[c] Department of Environmental Sciences, Faculty of Geosciences, Utrecht University, 3508 TA, Utrecht, The Netherlands
[d] Biogeochemical Processes Department, Max Planck Institute for Biogeochemistry, Jena, Germany
[e] Department of Physics, Federal Institute of Para, Belém, Brazil
[f] Climate and Atmosphere Research Center, The Cyprus Institute, Nicosia, Cyprus

ARTICLE INFO

Keywords:
Evapotranspiration
Net ecosystem exchange
Amazon rainforest
Multi-layer canopy

ABSTRACT

We studied the sub-hourly variability of water and CO_2 fluxes within and above the Amazon tropical forest during the dry season. Our aim was to investigate how forest layers contribute to the net ecosystem exchange (NEE) and evapotranspiration (ET) by accounting for the existing vertical profiles of leaf traits and microclimate, and the presence of clouds. To this end, we estimated NEE and ET with a 3-layer land-surface model driven by vertical profiles observed at the Amazon Tall Tower Observatory (ATTO) site during CloudRoots-Amazon22 field campaign. Our analysis focused on a typical "shallow-convective" day, composed of 6 individual days with similar conditions. The observed vertical profiles characterized microclimatic variables (photosynthetic active radiation, air temperature, humidity, CO_2, wind and turbulence) as well as leaf traits (maximum carboxylation rate, V_{cmax}; maximum electron transport, J_{max}; and ^{13}C leaf isotopic composition, $\delta^{13}C_p$) across three layers that represented the understory, the mid-canopy and the forest top-crown. The modeled NEE and ET were subsequently compared with eddy-covariance (EC) fluxes observed above the canopy.

We found distinctive vertical profiles of leaf traits and microclimate that were maintained during most of the day. In particular, we observed a persistent inversion of temperature within the canopy which hindered air mixing between the top-crown and the lower layers. Modeled NEE and ET fluxes were comparable in magnitude to the EC-measured fluxes, with flux dynamics dominated by the exchange of the top-crown layer. However, differences between observed and modeled NEE emerged during the morning transition (from 7:30 to 9:00 LT), when CO_2 stored within the canopy overnight was released. We conclude that tropical forests exhibit complex, distinctive vertical profiles of microclimate and leaf traits that influence the water and CO_2 vegetation exchange and the transport of air within the canopy.

1. Introduction

Forests interact with the atmosphere through exchanges of water, CO_2, energy and momentum, setting up a characteristic microclimate inside and above the vegetation layer (Finnigan et al., 2009; Belcher et al., 2012). Properly accounting for these forest-atmospheric interactions is vital to understand and quantify the biospheric compound of the terrestrial carbon and water cycles (Gentine et al., 2019). This can be particularly relevant in tropical regions because of their importance to the global hydrological and carbon cycles (Anav et al., 2015), because of the current uncertainty in their response to climate change (Friedlingstein et al., 2006; Davidson et al., 2012), and because tropical forests are dense and with large complex vertical variability (Shuttleworth et al., 1989). Traditionally, land-surface parameterizations have simplified the vertical extension of forests by representing them as a single vegetation layer (known as big leaf approaches) or, at most, as a single layer with sun-lit and shaded portions (known as two big leaf approaches) (Raupach and Finnigan, 1988; Bonan et al., 2021). In the past, these simplifications have been instrumental for advancing our understanding of land-atmosphere interactions. Nowadays, increasing model capabilities and availability of within-canopy observational datasets is enabling a more detailed

* Corresponding author.
E-mail address: raquel.gonzalezarmas@wur.nl (R. González-Armas).

https://doi.org/10.1016/j.agrformet.2025.110621
Received 13 December 2024; Received in revised form 28 April 2025; Accepted 10 May 2025
Available online 10 June 2025

description of the within-canopy microclimate, leaf traits and forest canopy architecture, thereby fostering an improved understanding of forest-atmospheric interactions (Bonan et al., 2021).

Exchanges and interactions between the forest and the atmosphere are governed by processes that operate at the subdiurnal time-scale (Seo and Dirmeyer, 2022). Some of them are the solar diurnal irradiance pattern, the growth of the convective boundary layer, the distinct turbulence regimes, the entrainment of air from the free troposphere into the atmospheric boundary layer (ABL), and the presence of clouds (such as shallow-cumulus clouds) which are coupled to the ABL state. A realistic characterization of the subdiurnal time-scale is also important for atmospheric inversion models and remote sensing applications, for example, for relating remote sensing measurements of sun-induced fluorescence to canopy photosynthesis (Sun et al., 2015).

A large body of research has focused on characterizing particular subdiurnal features of microclimate (Shuttleworth, 1984, 1985; Wofsy et al., 1988; Shuttleworth et al., 1989; Culf et al., 1997; Malhi et al., 1998; Kruijt et al., 2000; Santana et al., 2017; Parker et al., 2019), subdiurnal features of leaf and ecosystem gas exchange (Fitzjarrald et al., 1990; Dolman et al., 1991; Grace et al., 1995; Araújo et al., 2002), and the vertical gradients of leaf traits (Carswell et al., 2000; Lloyd et al., 2010) in the Amazon forest. However, few field-campaigns have measured them simultaneously and for multiple forest layers. A comprehensive study that combined observations of microclimate above the canopy, leaf gas exchange and leaf traits with a land-surface parameterization is that of Lloyd et al. (1995). They used a big-leaf approach, driven by the observed microclimate and leaf traits, to simulate the gross primary productivity (GPP) of an Amazonian forest, and they discussed the validity of the big-leaf approach in tropical forests.

In this study, we used a similar approach to that of Lloyd et al. (1995). However, key distinctions are the breakdown of the canopy into three forest layers, the use of microclimate observations measured within the canopy, and the calculation of both CO_2 and water fluxes. Our objective is not to compare big-leaf and multi-layer approaches. We consider that this topic has been extensively covered by, for instance, Raupach and Finnigan (1988) and recently by Bonan et al. (2021). Instead, we aim to derive water and CO_2 fluxes in three forest layers and to investigate the different vegetation-atmospheric dynamics at play in each layer, taking into account the fast cloud and canopy radiative perturbations at the subdiurnal scale. To this end, we analyzed and extended the comprehensive observational dataset measured at the Amazon Tall Tower Observatory (ATTO) during CloudRoots-Amazon22 field campaign (Vilà-Guerau de Arellano et al., 2024). In this manuscript, we first present a characterization of the observed microclimate and leaf traits during a typical "shallow-convective" day, composed of 6 individual days with similar conditions. Subsequently, we analyzed in depth the results of a three-layer model that is driven by the observed profiles of microclimate and leaf traits. Finally, we compare and discuss the ecosystem fluxes of the observational-driven three layer-model with respect to those observed by an eddy-covariance (EC) system located above the forest.

2. Methods

2.1. Study site and CloudRoots-Amazon22 field campaign

Observations used in this study were acquired at ATTO (2° 8′ 45″ S, 59° 0′ 19″ W; Andreae et al., 2015) during the CloudRoots-Amazon22 field campaign (Vilà-Guerau de Arellano et al., 2024). The CloudRoots project explores the interactions between vegetation and atmosphere, and the role of clouds therein. The project adopts a bottom-up approach that integrates biophysical process understanding and observations from the leaf surfaces up to the ABL, or even the regional atmospheric scale (Vilà-Guerau de Arellano et al., 2023). CloudRoots-Amazon22 extends the general project approach to a tropical forest. The campaign added dedicated observations which, together with the continuous observations regularly acquired at the ATTO facility, allowed the characterization of the land-atmosphere system from the stomata (size of 10 to 100 μm) to the depth of the ABL (ca. 1 km). CloudRoots-Amazon22 campaign took place from August 8 to 21, 2022 (Southern Hemisphere Amazon dry season) at and around the measurement sites of ATTO and a nearby observatory called Campina (2° 10′ 55″ S, 59° 1′ 18″ W). For more details about the campaign, see Vilà-Guerau de Arellano et al. (2024).

An extensive documentation about ATTO research facility can be found in Andreae et al. (2015). Here, we summarize some relevant features of the site. The ATTO site is located 150 km northeast of Manaus (Brazil) and approximately 1000 km inland and downwind from the Atlantic Ocean. It is located at 120 m.a.s.l. on a plateau of terra firme (i.e., non-flooded upland) pristine forest. The mean tree height is 20.7 ± 0.4 m but the tallest trees reach up to 36–40 m. The ATTO facility consists of three towers: ATTO tall tower (ca. 323 m), a triangular tower (ca. 100 m) and the Instant tower (ca. 80 m). Sensors placed at the towers continuously monitor key atmospheric variables (e.g., radiation, temperature, humidity, wind), trace gases (e.g. CO_2, CH_4), chemically reactive species and turbulent fluxes. In this study, we exclusively used data from the Instant tower because that tower was densely surrounded by vegetation, being fully integrated into the forest structure, and it had several radiation sensors within and above the canopy.

During CloudRoots-Amazon22, all days were characterized by shallow-cumulus clouds, which appeared at approximately 9–10 LT. Shallow-cumulus clouds are ubiquitous in the Amazon rainforest (Giangrande et al., 2017). Their onset is related to the transition of the nocturnal stable atmospheric boundary layer into a convective boundary layer (Henkes et al., 2021), which normally occurs between 8–9 and 11 LT. To organize the CloudRoots-Amazon22 days, we followed the regime classification developed by Henkes et al. (2021) which distinguishes between (1) shallow-convective days and (2) shallow-to-deep convective days. This classification was already used for the CloudRoots field campaign in Vilà-Guerau de Arellano et al. (2024) (see Table 2 therein for details). In this study, we focused exclusively on the shallow-convective days. These days were August 9, 10, 11, 15, 17 and 18, 2022. We present results for a composite "shallow-convective" day created by averaging each variable across the 6 individual shallow-convective days.

2.2. Observations

2.2.1. Microclimate

The microclimate inside and above the canopy was characterized by vertical profiles and temporal series of photosynthetic active radiation (PAR), air temperature (T), relative humidity (RH), vapor pressure deficit (VPD), atmospheric CO_2 concentration (C_a), horizontal wind-speed (U) and turbulence kinetic energy (TKE). Additionally, observed long-wave outgoing radiation (LW_{out}) was use to derive the surface skin temperature based on Stephan-Boltzman equation for an emissivity of $\epsilon = 1$. Table 1 indicates the instruments that measured each variable together with the time frequency of the sensor and the heights where the sensors were deployed.

In the vertical profiles, we indicated the aerodynamic height of the canopy. The aerodynamic height (h_a) was calculated as the inflection point on the vertical wind profile using a similar procedure as Thomas and Foken (2007). To obtain a smooth wind vertical profile, we fitted a piecewise cubic polynomial that was twice continuously differentiable to the wind vertical profile.

To have a reference of clear-sky radiation, we used the McClear version 4.6 product (Lefèvre et al., 2019) from the Copernicus Atmosphere Monitoring Service (CAMS). CAMS McClear includes corrections based on atmospheric composition from re-analysis data, such as aerosol concentration and total column atmospheric water vapor. This estimation

Table 1
Microclimatic variables within and above the forest. The heights of the observations used as input for the 3-layer land-surface model appear in **bold** font. RH and VPD at 4 m was calculated from the measurements of H_2O concentration (Picarro L2140-i), air temperature and air pressure. The H_2O concentration measurements at 4 m were only available for a subset of the composite days (August 17 and 18 2022). The G2401 system measures CO_2 concentration over a buffer system (Winderlich et al., 2010; Botía et al., 2020).

Variable	Instrument	Time frequency	Height
PAR (incoming)	Quantum sensor (PAR LITE, Kipp & Zonen, The Netherlands)	1 min	**5**, **15**, **25**, 35, 50, 81 m
PAR (incoming)	FROST[a] (Heusinkveld et al., 2023)	1 s	0.5, 5, 15, 23, 63 m
Air T and RH	Thermohygrometer (IAKM, Galltec, Germany)	1 min	**26**, 36, 55, 73, 81 m
Air T	Thermometer (Hmt337, Vaisala, Finland)	1 min	**4**, **12** m
H_2O concentration	Picarro (L2140-i, Picarro Inc., Santa Clara, CA, USA)	≈24 min	**4** m
CO_2 concentration	Picarro (G2401, Picarro Inc., Santa Clara, CA, USA)	30 min	**4**, **24**, 38, 53, 79 m
U and TKE	3D Ultrasonic Anemometer (CSAT-3b, Campbell Scientific Instrument Inc., USA)	30 min	5, 25, 50, 81 m
U and TKE	3D Ultrasonic Anemometer (THIES, Germany)	30 min	15, 35 m
LW_{out}	Pyrgeometer (CGR4, Kip & Zonen, Netherlands)	10 min	75 m

[a] It should be noted that the FROST instruments are not part of the continuous ATTO observation network; they were brought exclusively for the field campaign.

allowed us to describe the above-canopy radiative perturbations caused solely by clouds. The only further processing applied to the CAMS McClear product was the conversion from global horizontal irradiance (GHI) to PAR. To derive this conversion, we use GHI and PAR observed by a spectroradiometer (FROST instrument; Heusinkveld et al., 2023) above the canopy (at 63 m). The observations indicated a conversion of PAR = 0.4400·GHI, Fig. A.9.

2.2.2. Leaf traits and leaf gas exchange

To characterize the vertical variability of leaf traits, we divided our measurements over three roughly equally spaced canopy layers: understory (0–10 m), mid-canopy (10–20 m) and top-crown (20–30 m). To characterize the leaf traits of each layer, we carried out two type of measurements: photosynthesis response curves to internal CO_2 concentration (known as A-C_i response curves) and ^{13}C carbon isotope analysis. A-C_i response curves were measured with an LI-6400 XT portable photosynthesis system (Licor Inc., Lincoln, NA, USA). We measured A-C_i curves on randomly chosen leaves from trees and understory vegetation surrounding the Instant tower. Once the tree was selected, a professional tree climber climbed to the desired height, cut a branch of approximately 1 m in length and let it fall to the forest floor. Then, we measured the A-C_i response curves at saturating light (≈2000 μmol m^{-2} s^{-1}) following (Evans and Santiago, 2014). In total, we measured 8 A-C_i response curves in the understory, 9 in the mid-canopy and 9 in the top-crown (Fig. B.11).

For each of the curves, we derived model parameters according to two leaf gas exchange models. The first model was the Farquhar, von Caemmerer and Berry model (Farquhar et al., 1980) from which we estimated the maximum velocity of carboxylase ($V_{c,max}$) and the maximum rate of electron transport (J_{max}). The second model was the A-g_s model (Jacobs, 1994) and we estimated the maximum leaf photosynthetic capacity at 298 K ($A_{mmax298}$) and the mesophyll conductance at 298 K (g_{m298}). Both models proved capable of representing the measured response curves, which is consistent with a thorough comparison between the two models (van Diepen et al., 2022) that reports that both models simulate similar photosynthetic response curves.

In addition to the A-C_i response curves, stomatal conductance was measured using the LI-6400XT system in five periods centered around solar noon (6:00-7:30 LT, 8:30-10:00 LT, 11:15-12:45 LT, 14:00-15:30 LT and 16:30-18:00 LT), during two consecutive days (August 11 and 12, 2022). We measured 6 leaves (when possible 3 sun-lit and 3 shaded) per layer and time period. For these measurements, we measured leaves that were accessible from the Instant tower or from the ground. Once a tree was selected, we cut small branches (of approximately 30 cm), let them fall to the forest floor and immediately performed the measurements at the ground level of the forest where we had our instrumental set-up. The chamber head of the LI-6400XT system was closed, so we had to set the environmental conditions inside the chamber. To set a realistic radiation, we measured radiation with a LAI ceptometer (ACCUPAR LP-80, Meter) that is composed by a linear array of PAR sensors. For each forest layer, we measured radiation according to two light treatments: shaded and sun-lit spots, and we measured 8 times for each treatment at several horizontal orientations. Lastly, the (sun-lit or shaded) averaged measured radiation was set in the closed chamber to measure the stomatal conductance of a (sun-lit or shaded) leaf.

The second type of observations that characterized the leaf traits were ^{13}C carbon isotope analysis. First, we sampled the leaves in which we measured the A-C_i curves and some additional leaves that were selected in the same manner as the leaves for the A-C_i curves. In total, we sampled 56 leaves (19 in the understory, 18 in the mid-canopy and 19 in the top-crown). After collection, the leaves were first dried in an oven at 60 °C for the following 48 h and then stored in sealed bags to keep them dry. A few days later, leaves were manually ground at the National Institute of Amazonian Research (INPA) and stored in plastic centrifugal tubes for export. After re-drying them at 60 °C for 12 h at the GeoLab in Utrecht University, fine grinding was performed using a Mixer Mill for 120 s per sample. Then, we prepared the fine ground samples for the isotope analysis by placing 1000–1500 μg of leaf material in tiny aluminum cups. Finally, the isotope measurements were performed with a EA-IRMS (Elemental Analyzer – Isotope Ratio Mass Spectrometer) instrument with IAEA-CH-7 as the ^{13}C reference standard.

Based on the ^{13}C isotopic measurements, we estimated the ratio of internal sub-stomatal CO_2 (C_i) to atmospheric CO_2 mixing ratios (C_a). To that aim, we employed the following expression in accordance to Farquhar et al. (1989):

$$\frac{C_i}{C_a} = \frac{\Delta^{13}C - a}{b - a} \tag{1}$$

where a (4.4‰) and b (28‰) are constants representing the fractionation due to diffusion and carboxylation, respectively, (Farquhar et al., 1982) and $\Delta^{13}C$ is the carbon discrimination calculated following Farquhar et al. (1989) as:

$$\Delta^{13}C = \frac{\delta_a^{13}C - \delta_p^{13}C}{1 + \delta_p^{13}C} \tag{2}$$

where $\delta_a^{13}C$ and $\delta_p^{13}C$ are the ^{13}C isotopic composition of the atmospheric CO_2 and of the carbon in the leaf material with respect to the Vienna Peedee Belemnite (VPDB) isotope reference. The atmospheric isotopic composition, $\delta_a^{13}C$, was measured during CloudRoots-Amazon22 field campaign. Measurements were available right above the canopy (38 and 42 m), at the top-crown (24 m) and in the understory (4 m) (for details about the instruments, see Vilà-Guerau de Arellano et al., 2024). To use a unique diurnal value per layer, we averaged the observations during the days with shallow-convection, which are presented in Vilà-Guerau de Arellano et al. (2024) (Fig. 4 therein). For the top-crown layer we used the observations from 24 and 38 m, for the mid-canopy we used the values from 4 and 24 m and for the understory we used the values from 4 m. The values for the top-crown, mid-canopy and understory were respectively −9.14‰, −9.69‰, and −10.23‰.

2.2.3. Ecosystem fluxes

An eddy covariance system was used to calculate the surface turbulent fluxes of water and CO_2 (F_{H_2O} and F_{CO_2}) above the forest (at 50 m.a.g.l $\approx 1.5h_a$) for 30 min intervals. Three-dimensional wind and temperature fluctuations were measured by a sonic anemometer (instrument details in Table 1). CO_2 and H_2O fluctuations were measured by three fast response closed-path CO_2 /H_2O infrared gas analyzers (IRGA LI-7200) installed at a lateral distance of about 10 cm from the sonic path. The high-frequency signals were recorded at 10 Hz by CR1000X data logger. The raw data was processed applying the software EddyPro (Biosciences, 2019). Fluxes, means and variances were calculated for half-hourly intervals. The vertical turbulent transport measured by the EC-system does not necessarily equal the ecosystem exchange (defined as the sum of emissions and/or uptake by the vegetation and soil) because water and CO_2 can be stored in the air layer below the sensor (Foken et al., 2012). This effect was quantified by the storage flux term, $F_{stor,\chi}$ with χ being water vapor or CO_2. The storage terms were calculated as:

$$F_{stor,\chi} = \int_0^h \frac{\rho_d}{M_d} \frac{\partial \chi}{\partial t} dz, \tag{3}$$

with h being the height of the EC system where turbulent fluxes are observed, ρ_d the dry air density and M_d the molecular weight of dry air. To estimate the integral in height, we used 4 sensors that measured humidity (at 4, 26, 36 and 55 m) and CO_2 concentration (at 4, 24, 38 and 53 m). Finally, the observed ecosystem fluxes – the net ecosystem exchange (NEE_{obs}) and evapotranspiration (ET_{obs}) – were estimated as the sum of the surface turbulent fluxes and the storage fluxes:

$$NEE_{obs} = F_{CO_2} + F_{stor,CO_2} \tag{4}$$

$$ET_{obs} = F_{H_2O} + F_{stor,q} \tag{5}$$

Soil respiration (CO_2 emission flux) was also measured close to the ATTO tall tower using an automated closed dynamic soil flux measuring system (Licor Inc., Lincoln, NA, USA). The system consisted of an infrared gas analyzer (LI-870), a 8-port multiplexer (LI-8250) and 3 dynamic long-term chambers with opaque lids (LI 8200-104). The flux measurements of each chamber consisted of: 1.5 min of pre-purge during which the chamber lid was opened and lines flushed with ambient air, 4 min of closure time, and 1 min of post-purge. The three chambers measured consecutively, and the soil CO_2 flux was calculated by applying an exponential model to the CO_2 concentration during the chamber closure period (Pugliese et al., 2023). The three chambers were placed on PVC-collars (Ø: 19.4 cm) installed on three types of surfaces: bare organic soil, bare clay soil and clay soil with litter. To characterize the diurnal surface respiration we averaged the measurements over the three surface types.

Additionally, observed friction velocity (u_*) and sensible heat flux (H) at 50 m were used to define a morning transition from the nocturnal ABL to a well-mixed ABL, Fig. C.13. The morning transition was defined as the period between the time when the sensible heat flux became positive and the time when the friction velocity stabilized (Dupont et al., 2024).

2.3. Three-layer model

At each layer (understory, mid-canopy and top-crown), we represented the leaf gas exchange (stomatal conductance, net CO_2 leaf assimilation, leaf transpiration and C_i) with the A-g_s model (Goudriaan et al., 1985; Jacobs, 1994). The model described the observed leaf traits since it included the measured vertical profiles of mesophyll conductance and maximum assimilation rate at 298 K. Furthermore, the model used as input the observed vertical profiles and time series of PAR, T, VPD and CO_2. Because no observations of VPD and CO_2 were available at the mid-canopy, VPD and CO_2 were linearly interpolated at 15 m from the available observations in the understory and top-crown. Additionally, CO_2 observations were linearly interpolated in time to match the 1 min resolution of the other observations.

To up-scale from leaf fluxes to canopy fluxes, we used the 3-point Gaussian quadrature approach (Goudriaan, 1986). Details about the approach can be found in Appendix D. In that approach, we considered a leaf area index (LAI) of 5.32 m^2 m^{-2} in accordance to the value reported by Gomes Alves et al. (2023) for the ATTO site. By up-scaling the fluxes, we estimated the CO_2 assimilation (A_n) and transpiration (TR) of the individual forest layers and of the whole vegetation canopy.

Apart from the vegetation fluxes, we calculated the water use efficiency (WUE) defined as the ratio between A_n (defined as positive if CO_2 is taken up by the plant) and TR. Finally, the up-scaled fluxes were compared with those observed (Eqs. (4) and (5)). To be able to compare them, we needed to include the soil contribution to the up-scaled fluxes. We did so by including the observed soil respiration to the up-scaled net CO_2 assimilation and assuming negligible soil evaporation.

3. Results

3.1. Vertical profiles of microclimate and leaf traits

3.1.1. Radiation

Incoming PAR above the canopy followed a diurnal pattern that was perturbed by the presence of shallow-cumulus clouds (Fig. 1a). The shallow-cumulus clouds were present from approximately 9:45 and their net diurnal effect was to diminish incoming radiation compared to clear sky values by 6.2 ± 2.3%. During 40% of the day we observed cloud shadows (Fig. A.10), which reduced radiation by approximately 14% on average. During 13% of the time, we observed enhancement of radiation due to the increased diffuse radiation from nearby clouds edges, which increased radiation by approximately 4% on average.

PAR measured inside the top-crown layer of the canopy was slightly reduced but still highly correlated with PAR above the canopy (r^2 = 0.95). Consequently, the cloud-induced radiative perturbations affected the photosynthesis in the top-crown leaves. From 6:00 to 7:30 LT and from 15:30 to 18:00 LT, PAR measured at the top-crown was significantly lower than that measured above the canopy, most probably due to the high solar zenith angle. When the solar zenith angle is high, the direct light beam travels longer until reaching a certain height within the canopy, increasing the chances for light to encounter obstacles such as leaves and branches. Additionally, the anisotropy of the plant material around the radiation sensor can create shades at particular moments of the day. For instance, between 15:30 and 17:00, the top-crown sensor was likely shaded by some big and opaque object such as a trunk because it registered the same values across the 6 days (showing a small standard deviation across days). In the mid-canopy, radiation was reduced to, on average, 7% of the above canopy radiation. Most of the mid-canopy radiation was received close to noon (between 10:30 and 12:00 LT). The higher radiation received at noon is likely related to the creation of a small clearing when the solar zenith angle is low. In the understory, radiation was minimal; only 0.7% of the above canopy radiation reached the sensor located at 5 m height.

Observed PAR attenuated inside of the canopy abruptly between 25 and 15 m and moderately below 15 m (Fig. 1b, c and d). The variability of the observed PAR intensity during the 1.5 h time periods (black error bars) was higher than the day-to-day variability (red error bars). This indicates that the observed PAR intensity varied more due to the diurnal cycle of radiation than due to the differences between individual days. The observed PAR vertical profiles seemed generally consistent with the exponential Beer–Lambert law of light extinction of a fitted extinction coefficient K_x = 0.65 and LAI = 5.32 m^2 m^{-2} (leaf area density in Fig. D.15), although the observed profile showed a steeper radiative attenuation between 25 m and 15 m at all time intervals.

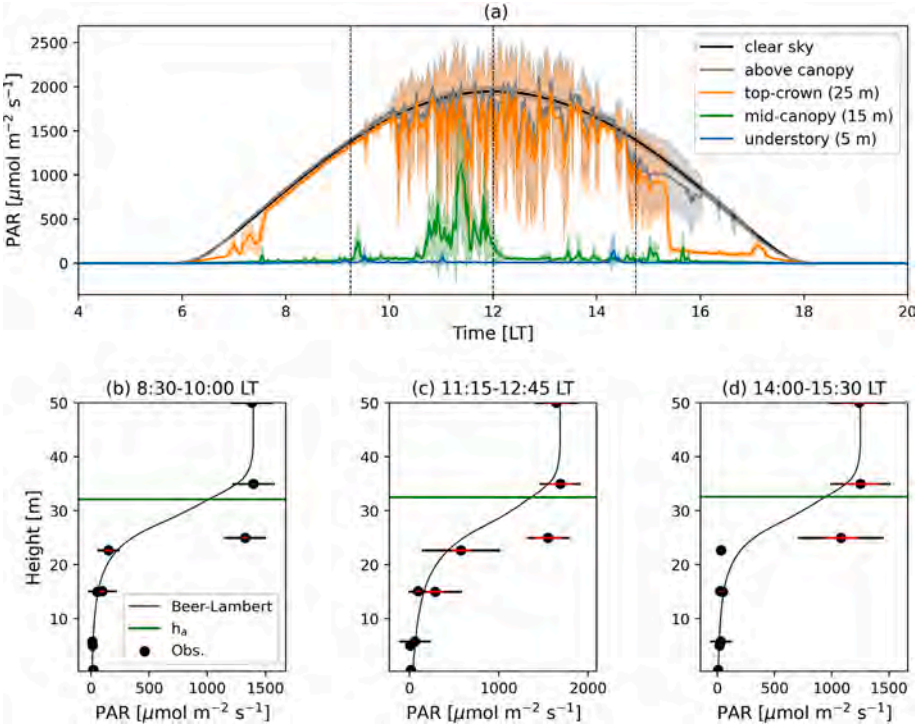

Fig. 1. Panel (a) depicts the time series of observed PAR (above the canopy, at 25 m, 15 m and 5 m) and a clear-sky reference for the composite day. The solid lines represent the mean value whereas the shaded region indicates the range within one standard deviation. Panels (b), (c) and (d) are vertical profiles of observed PAR. Two standard deviations of the observations are shown, the black error bar show the standard deviation during the time periods whereas red error bars show the standard deviation across the individual days that constitute the composite. Additionally, panels (b), (c) and (d) show the Beer–Lambert extinction profile of $K_x = 0.65$, LAI = 5.32 m^2 m^{-2} and leaf area density as indicated in Fig. D.15. Aerodynamic canopy height is indicated as a green horizontal line.

3.1.2. Temperature, humidity and CO_2

Vertical profiles of air temperature (Fig. 2a) indicated the presence of a stable layer within the canopy during daytime. This stable layer was characterized by a temperature maximum above the canopy (from 6 to 7:30 LT and from 16:30 to 18:00 LT) or at the top-crown layer (from 8:30 to 15:30 LT) and decreasing temperatures with canopy depth. The temperature inversion was generally slightly stronger in the understory than in the mid-canopy. The temperature range within the canopy was approximately 2 °C at the beginning of the day and 3–4 °C during the rest of the day. The highest air temperatures found at the top-crown canopy (from 8:30 to 15:30 LT) are associated with the outgoing sensible heat flux from the warm sun-lit leaf surfaces of the top-crown layer. The skin temperature derived from the terrestrial long-wave radiation was generally higher than the temperature at the top-crown (by up to 1 °C), suggesting higher leaf temperatures than atmospheric temperatures at this canopy layer. The day-to-day air temperature variability was similar to the variability during the 1.5 h intervals, and generally smaller than the vertical variability. The largest day-to-day air temperature variability occurred from 6:00 to 7:30 LT, suggesting the influence of individual nighttime conditions on the early morning vertical profiles of air temperature.

We observed a clear separation in VPD and RH between the understory and top-crown layer (Fig. 2b) since 8:30 LT. Comparing the understory with the top-crown and above canopy sensors, we observed a difference of approximately 500–750 Pa in VPD and of approximately 5%–15% in RH. Despite the differences, both top-crown and understory sensors depicted a diurnal cycle in which VPD increased until reaching a maximum at 14:00-15:30 LT and then decreased until sunset. The opposite occurred for RH which decreased until reaching a minimum at 14:00-15:30 LT and then increased until sunset.

Atmospheric CO_2 showed a vertical profile with CO_2 maxima near the forest floor during all time intervals (Fig. 2c). In the understory, the highest CO_2 values were observed during the two early time intervals (from 6:00 to 10:00 LT). During these moments, differences between understory and above canopy CO_2 were approximately 30–40 ppm. From 11:15 to 15:30 LT the difference in CO_2 between understory and above canopy air was smaller (approximately 20 ppm) but it increased again (to approximately 30 ppm) in the late afternoon (from 16:30 to 18:00 LT). Similarly to air temperature, the day-to-day variability was largest from 6:00 to 7:00 LT, suggesting the influence of individual nighttime conditions on the early morning vertical profiles of CO_2.

3.1.3. Wind and turbulence

Atmospheric variables related to the mixing of air also changed with height and time (Fig. 3). Wind attenuated near and within the canopy following the widespread assumption of a logarithmic decay above the canopy and an exponential decay within the canopy (Fig. 3a). The aerodynamic height, defined as the inflection point of the wind speed vertical profile, was 33.7 m ± 1.2 m. The turbulent kinetic energy varied throughout the day, showing the highest values between 11:15 and 15:50 (Fig. 3b). Similarly to the wind profile, its decay inside the canopy resembled an exponential function with great attenuation in the upper half of the canopy.

3.1.4. Leaf traits

Leaf traits showed distinct vertical gradients within the canopy, Fig. 4 and Table B.3. Observed $V_{c,max}$ and J_{max} increased with height from the understory to the top-crown canopy by 20 μmol m^{-2} s^{-1} and 50 μmol m^{-2} s^{-1} respectively, Fig. 4a and b. The leaf ^{13}C isotopic composition, $(\delta_p^{13}C)_{VPDB}$, increased with height with a difference of 3.75‰ between understory and top-crown canopy, Fig. 4c. The C_i/C_a ratios derived from the $\delta_p^{13}C$ observations exhibited an opposite vertical profile with lower ratios higher in the canopy, Fig. 4d. These ratios suggest greater CO_2 leaf assimilation rates higher in the canopy. This is in line with the greater radiation (Fig. 1), $V_{c,max}$ (Fig. 4a) and J_{max} (Fig. 4b) observed at the top-crown canopy.

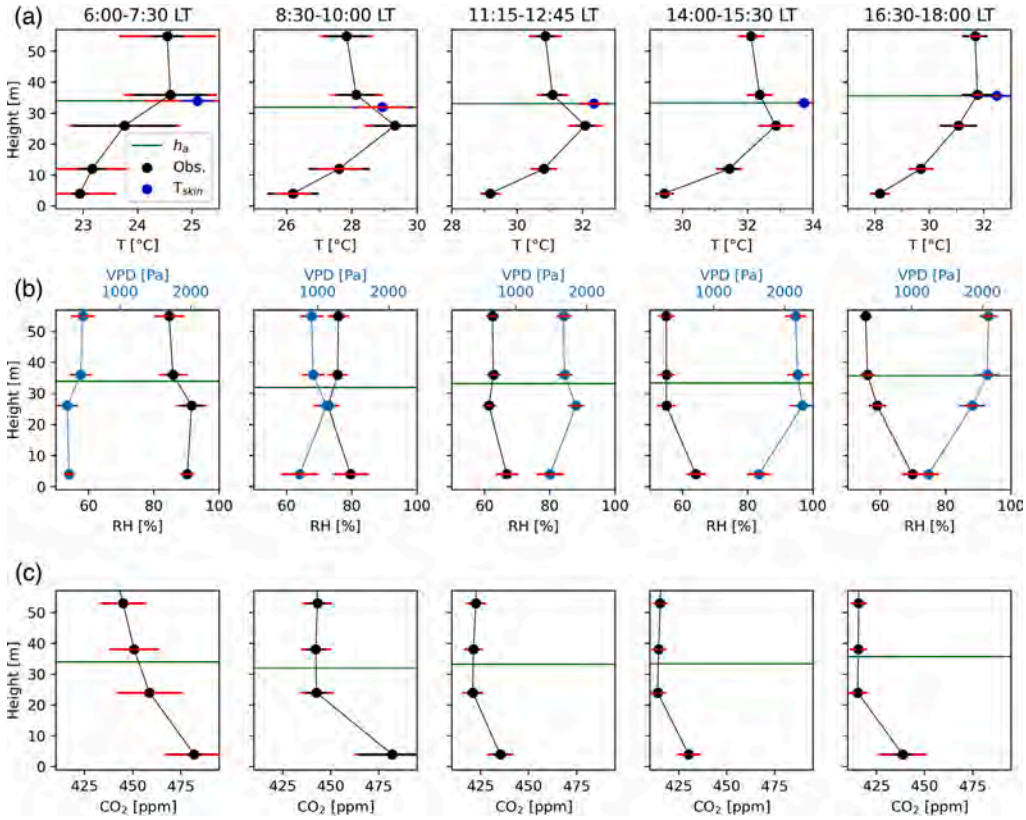

Fig. 2. Vertical profiles of observed: air temperature (a), vapor pressure deficit and relative humidity (b), and atmospheric carbon dioxide (c). Profiles are shown for the composite day for 5 time intervals: from 6:00 to 7:30 LT, from 8:30 to 10:00 LT, from 11:15 to 12:45 LT, from 14:00 to 15:30 LT and, from 16:30 to 18:00 LT. Black (or blue for skin temperature and VPD) error bars show the standard deviation during the interval time for the averaged observation whereas red error bars show the standard deviation across the individual days that constitute the composite. Aerodynamic canopy height is indicated as a green horizontal line.

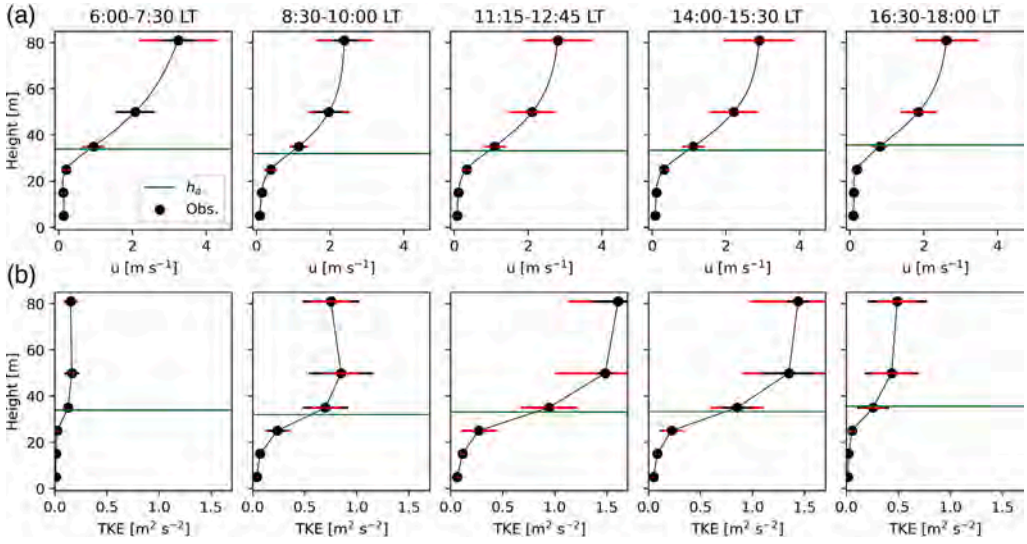

Fig. 3. Vertical profiles of observed: wind speed (a) and turbulent kinetic energy (b). Profiles are shown for 5 different times of the composite day: from 6:00 to 7:30 LT, from 8:30 to 10:00 LT, from 11:15 to 12:45 LT, from 14:00 to 15:30 LT, and from 16:30 to 18:00 LT. Black error bars show the standard deviation during the time interval for the composite vertical profile whereas red error bars show the standard deviation across the individual days that constitute the composite. Aerodynamic canopy height is indicated as a green horizontal line.

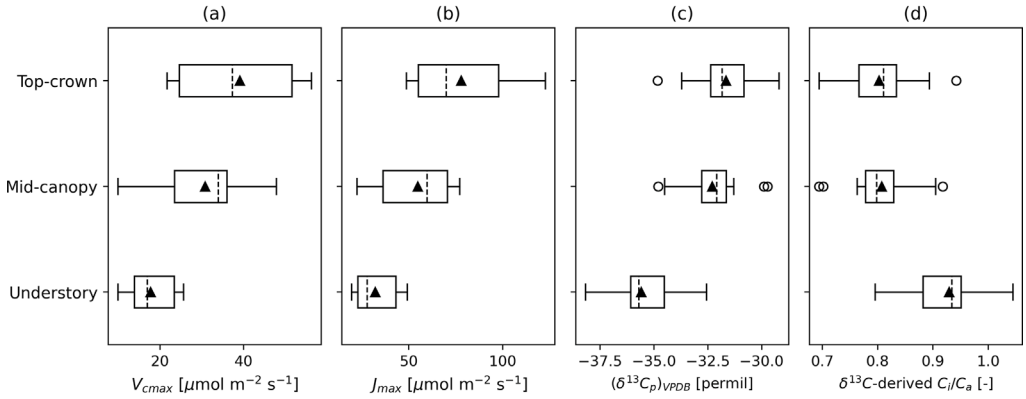

Fig. 4. Vertical profiles of: (a) $V_{c,max}$, (b) J_{max}, (c) leaf ^{13}C isotopic composition, $(\delta^{13}_{p}C)_{VPDB}$, and (d) $\delta^{13}C$-derived C_i/C_a ratio. Black triangles depict mean values whereas dashed black lines depict the median.

3.2. Modeled and observed leaf gas exchange

Observed and modeled C_i/C_a ratios showed a diurnal cycle (Fig. 5a) with a marked vertical gradient during daytime (Fig. 5b). The gradient, depicting lower C_i/C_a ratios higher in the canopy, was milder for the modeled results than for the two observational sets: the $\delta^{13}C$-derived measurements and the leaf gas exchange measurements. The observed and modeled diurnal cycle of C_i/C_a (Fig. 5a) was characterized by a decline until achieving minimum values between 14 and 16 LT, followed by an increase until sunset. The C_i/C_a ratio showed an opposite diurnal cycle than VPD, with lower C_i/C_a ratios with higher VPD (Fig. 2b). Model results and observations differed most around sunrise and sunset, when observed ratios were larger than modeled results.

Stomatal conductance (Fig. 6) also showed a diurnal cycle with a strong vertical gradient, indicating larger stomatal conductance higher in the canopy. For both model and observations, stomatal conductance was larger at all moments in the top-crown that in the mid-canopy and understory. In the top-crown layer, the modeled results depicted a steep stomatal aperture at 7 LT that continued at a slower rate until reaching maximum values of 0.4 mol m^{-2} s^{-1} at 10 LT. Afterwards, the modeled stomatal conductance fluctuated due to the radiative cloud perturbations. The modeled top-crown stomatal conductance corresponded well with the maximum sun-lit observations performed at that layer. The mean top-crown observations were smaller (approximately 0.2 mol m^{-2} s^{-1}) and had a large standard deviation (of approximately 0.1 mol m^{-2} s^{-1}). This highlights the large variability in observed stomatal conductance that occurs within the top-crown. The modeled and observed mid-canopy stomatal conductance had similar values. Modeled mid-canopy stomatal conductance highly fluctuated in synchrony with the radiation perturbations experienced in that layer (Fig. 1a) which are the result of the diurnal PAR cycle, the light extinction, the cloud radiative perturbations and the canopy shading. In the understory, the modeled stomatal conductance underestimated the observed one. Modeled stomatal conductance in the understory was modest and only increased with occasional sun flecks.

3.3. Modeled and observed ecosystem fluxes

Similar to stomatal conductance, modeled A_n and TR showed a diurnal cycle that was most pronounced in the top-crown canopy, Fig. 7a and b. A_n and TR time series depicted temporal variability similar to that of the observed radiation (Fig. 1a). A_n was more symmetric around solar noon than TR because TR was importantly affected by the time series of VPD (Fig. 2b), which indicated higher VPD in the afternoon than in the morning.

Comparing the contributions of the different canopy layers, we observe that the top-crown layer dominated the whole vegetative canopy exchange (Fig. 7, Table 2). The mid-canopy layer had a lesser contribution, contributing 3% of the total vegetative canopy up-take and 19% of the total vegetative canopy transpiration (Table 2). But, even though the top-crown layer dominated the net daytime forest fluxes, the mid-canopy occasionally exchanged as much as the top-crown, especially when direct radiation penetrated deeper inside the canopy. This can be observed between 10:30 and 12:00 LT when both A_n and TR peaked (Fig. 7) at the same time that mid-canopy radiation was maximum (Fig. 1a). The understory had the lowest contribution to the total daytime vegetative canopy transpiration (3%). However, it contributed more than the mid-canopy to the total daytime CO_2 exchange. In contrast to the mid-canopy contribution, the modeled understory was a net diurnal source of CO_2 due to respiration processes, which accounted for 6% of the total diurnal CO_2 exchange in the vegetative canopy.

The water use efficiency (WUE), calculated as the ratio of the cumulative daytime A_n and the cumulative daytime TR, increased with height. Modeled WUE was large at the top-crown (10.18 g CO_2 kg^{-1} H_2O), low at the mid-canopy (1.95 g CO_2 kg^{-1} H_2O) and even negative for the understory (−15.14 g CO_2 kg^{-1} H_2O).

Considering soil respiration and assuming zero soil evaporation, we could obtain modeled NEE and ET. Modeled NEE and ET compared well with the observed NEE and ET in terms of the magnitude and diurnal pattern, particularly for ET, Fig. 8. Modeled and observed ET followed a similar diurnal pattern which grew quickly from about 1 h after sunrise, acquired maximum values between 11 and 15 LT and declined afterwards until sunset, Fig. 8b. Modeled and observed ET correlated well and significantly (r^2 = 0.95 and p-value < 0.001) and indicated similar cumulative evaporated water during daytime (Table E.4). Noticeable differences between modeled and observed NEE and ET occurred in two periods: midday (between 10:30 and 12:00 LT), and afternoon (between 15:30 and 17:00 LT). At midday, model results depicted an enhanced net CO_2 assimilation and transpiration compared to observations. The enhanced modeled fluxes are related to the local high radiation available in the mid-canopy at that moment (Fig. 1). The fluxes during this period reflect potential ecosystem exchanges, which may happen when radiation is able to penetrate further the canopy. In the afternoon, modeled results depict a dominance of respiration over assimilation (Fig. 8a) and a reduced evapotranspiration (Fig. 8b) which contrasts with the CO_2 assimilation and larger evapotranspiration suggested by observations. The discrepancy is due to the reduced observed radiation at the top-crown layer (Fig. 1a) due to a shade by a large and opaque object and it also reflects highly local conditions. As a consequence, during that periods modeled fluxes may not be representative of the whole canopy and should not be overemphasized.

Modeled and observed NEE showed a similar magnitude of maximum CO_2 up-take and a similar diurnal pattern. They correlated well and significantly (r^2 = 0.75 and p-value < 0.001). The diurnal cycle was characterized by positive values at nighttime (between 0 and

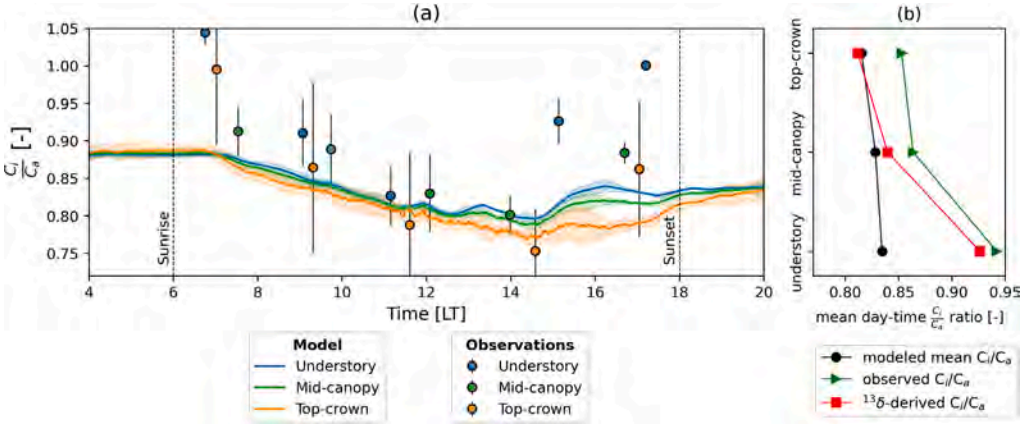

Fig. 5. (a) Time series of C_i/C_a ratio, and (b) vertical profiles of mean daytime C_i/C_a ratio. In panel (a), leaf gas exchange observations are shown with large circles with a black outline and an inner color that is: blue for the understory, green for mid-canopy and orange for top-crown. Leaf gas exchange observations have a vertical error bar that corresponds with the standard deviation. Model results are shown as lines with the same colors for each layer (blue, green and orange). The shaded area represents the range within one standard deviation of the modeled C_i/C_a ratio across the 6 individual shallow convective days. In panel (b), three vertical profiles are shown: the modeled profile (black line and circles), the profile observed through leaf gas exchange measurements (green line and triangles) and the profile derived from the $\delta^{13}C$ observations (red line and squares).

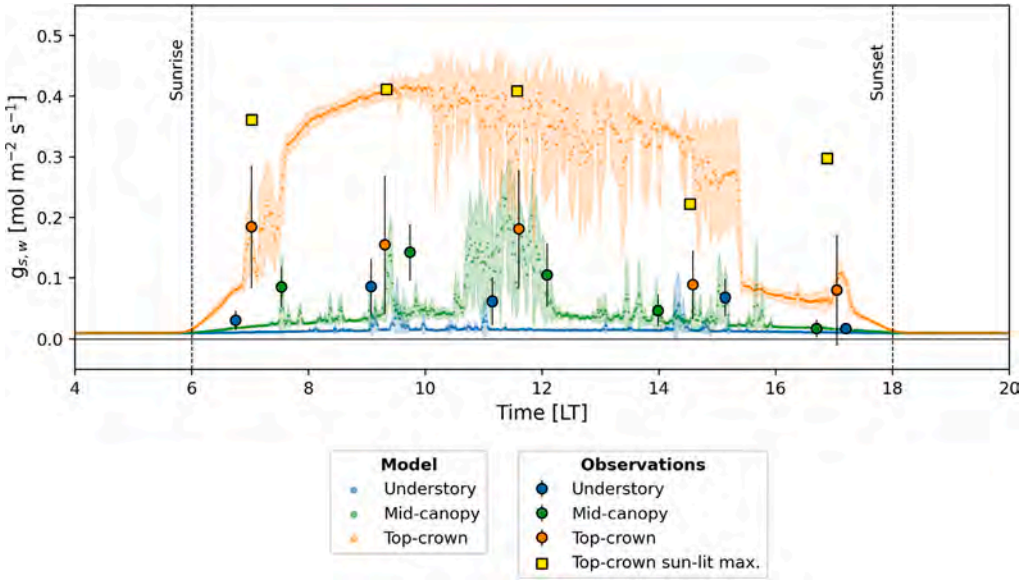

Fig. 6. Time series of stomatal conductance to water vapor. Leaf gas exchange observations are shown in circles with a black circumference and an inner color that is: blue for the understory, green for mid-canopy and orange for top-crown. Leaf gas exchange observations for each layer have a vertical error bar that corresponds to the standard deviation. Additionally, observed maximum stomatal conductance for the sun-lit leaves at the top-crown layer are shown in yellow squares. Model results are shown in smaller dots with the same colors per layer as observations (blue, green and orange). The shaded area represents the range within one standard deviation of the modeled stomatal conductance across the 6 individual shallow convective days.

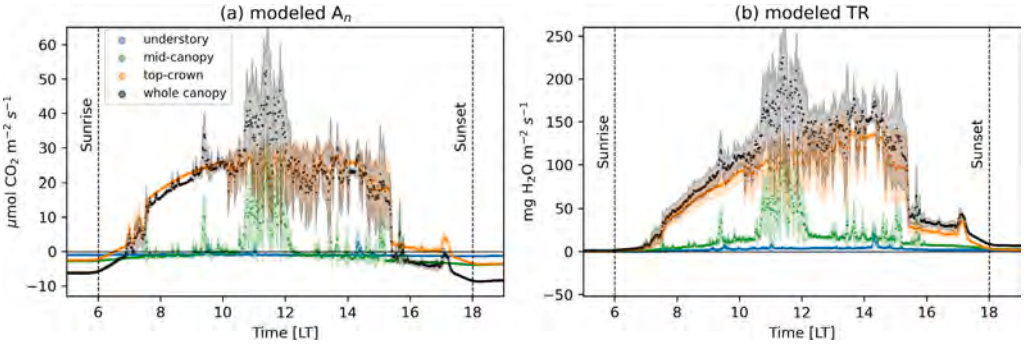

Fig. 7. Time series of modeled: (a) canopy net assimilation of CO_2 and (b) canopy transpiration. In each panel the total canopy flux appear in black dots whereas the contribution of each canopy layer to the net flux appear in: orange for top-crown, green for mid-canopy and blue for understory. The shaded area indicates the range within one standard deviation of the mean across the individual shallow convective days.

Table 2
Modeled cumulative CO_2 and water vegetation exchange per unit area during daytime for: the whole canopy, the top-crown, the mid-canopy and the understory. Between brackets it appears the percentage of the contribution of each layer to the total vegetation exchange. The percentage is negative for the understory contribution to the net canopy assimilation because the modeled understory was respiring CO_2 instead of assimilating it.

Variable	Units	Whole canopy (vegetation)	Top-crown	Mid-canopy	Understory
$\int_{sunrise}^{sunset} A_n \, dt$	g CO_2 m^{-2}	28.25 (100%)	29.15 (103%)	0.81 (3%)	−1.71 (−6%)
$\int_{sunrise}^{sunset} TR \, dt$	kg H_2O m^{-2}	3.77 (100%)	2.92 (78%)	0.72 (19%)	0.13 (3%)
WUE	g CO_2 kg^{-1} H_2O	7.50	9.99	1.11	−13.66

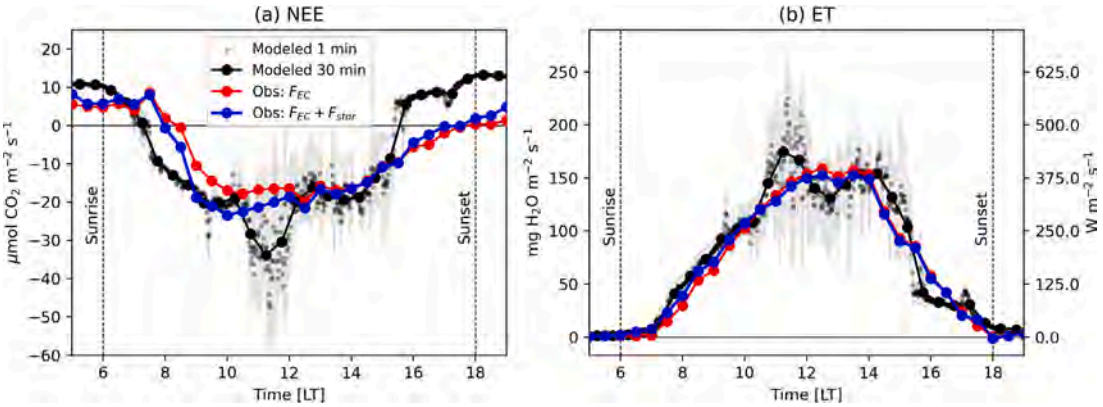

Fig. 8. Time series of: (a) NEE and (b) ET for the 6-day composite. 1-min modeled NEE and ET appear in grey small dots with a shade area that represents the range within one standard deviation across the 6 shallow convective days. 30-min modeled NEE and ET appear as black dots connected by a solid line. The 50 m observed NEE and ET appear as blue dots connected by a solid line. Observed NEE and ET are the sum of the surface turbulent fluxes measured by the EC-system (F_{EC}) and the storage terms (F_{stor}). The surface turbulent fluxes also appear as red dots connected by a solid line.

10 μmol CO_2 m^{-2} s^{-1}) corresponding with respiration processes and negative fluxes during daytime (of approximately 20 μmol CO_2 m^{-2} s^{-1} at noon) corresponding with a net assimilation of CO_2. Unlike for ET, a difference between modeled and observed results occurred in the early morning (between 7:30 and 9:00 LT). At 7:30, modeled NEE indicated a transition from the ecosystem being a net source of CO_2 (by respiring) to a sink (by assimilating). This transition was indicated by observations at 8:00 LT, half an hour later. Additionally, modeled results indicated larger assimilation rates from 7:30 until 9:00 LT. The effect of the storage term on the observations was noticeable, particularly in the morning (from 7:30 to 12 LT). By including the storage term, the respiration-assimilation transition shifted from 8:30 to 8:00 LT, getting closer to the modeled respiration-assimilation transition (7:30 LT). The morning, when we observed large observed-modeled NEE differences, is a interesting period. At that time, high CO_2 concentrations that were accumulated overnight within the canopy can be released by intense turbulent motions (Fig. 3) which occasionally penetrate the canopy. The resulting upward turbulent transport of enriched CO_2 air could offset the instantaneous net ecosystem uptake (what our model predicts) and result in a net positive turbulent flux (what the EC system measures). Remarkably, air transport seemed to play a lesser role for the water fluxes (Fig. 8b).

4. Discussion

The objective of this study was to investigate the vertical and subdiurnal variability of ET and NEE in the Amazon rainforest. Our discussion is structured in four sections. In the first section, we compare the observed microclimate and leaf traits with what has been reported by literature for dense tropical rainforests. In the second, we discuss how the within canopy horizontal heterogeneity of microclimate, particularly of radiation, affects modeled NEE and ET. In the third section, we comment on the contributions of each forest layer to the ecosystem fluxes, placing emphasis on the understory dynamics. In the final section, we discuss the modeled and observed ecosystem fluxes, focusing particularly on an intriguing period: the morning transition.

4.1. Microclimate and leaf traits

We found large vertical variability in microclimate and leaf traits within the canopy. The observed vertical profiles coincided with what has been previously reported in different studies for the region. In addition, the day-to-day variability of microclimatic variables was generally small, indicating robust and distinct vertical profiles. Radiation reaching the understory was found 0.7% of the above canopy radiation which is similar to the 1% reported by Shuttleworth (1984) for the forest floor of another Amazonian site. Temperature was found maximum at the canopy top and it decreased within canopy depth as reported by other studies (Shuttleworth, 1985; Kruijt et al., 2000). The temperature inversion within the canopy is indicative of an stable air layer. Such stable layers have been reported previously for the Amazon forest (Santana et al., 2018). In terms of relative humidity, we found higher relative humidity closer to the ground in agreement with a previous study (Shuttleworth, 1985). CO_2 mixing ratios were maximum at all times in the understory due to soil respiration which agrees with previous research (Wofsy et al., 1988). Turbulence attenuated sharply in the upper half of the canopy where it coexisted with the temperature inversion associated with a stable air layer. This characterization of turbulence shows similarities with previous studies by Kruijt et al. (2000) and Santana et al. (2018). The temperature inversion and low turbulence intensity at mid-canopy suggest a decoupling of the air from the lower half of the canopy with the air above, with turbulent motions unable to break the temperature gradients that hinder the within canopy air mixing during daytime (Vilà-Guerau de Arellano et al., 2023). Additionally, turbulence could not eliminate the gradients of other scalars such as CO_2 (Fig. 2), potentially affecting their residence times within the canopy, during these days characterized by shallow convection.

Regarding the leaf traits, both V_{cmax} and J_{max} increased with height within the canopy. V_{cmax} at the top-crown was roughly two times that at the understory and J_{max} at the top-crown was roughly about three times that at the understory. These gradients coincided with those reported by Carswell et al. (2000) who estimated the gradients measuring

two different tree species at four different heights in a nearby site. These vertical gradients in photosynthetic biochemistry likely reflect optimality in the investment of nitrogen and rubisco as a function of light intensity (Stocker et al., 2020; Harrison et al., 2021). Although the gradients corresponded well, we found slightly lower values than those reported by Carswell et al. (2000). Finally, we also found similar C_i/C_a ratios to Carswell et al. (2000), which often exceeded 0.8 (Figs. 4d and 5).

4.2. Horizontal heterogeneity

Our study covered key controlling variables of the water and CO_2 exchange at multiple heights within and above the canopy. Ecosystem fluxes were modeled using vertical profiles derived from in-canopy measurements collected at a single tower, assuming that these profiles are representative of the forest canopy. Although this assumption is likely valid for variables such as CO_2, VPD and temperature, which exhibit limited horizontal variation, radiation has significant horizontal heterogeneity (Anhuf and Rollenbeck, 2001; Parker et al., 2019). Rapid and intense fluctuations in radiation within the canopy were observed, driven by factors such as cloud passages, leaf flutter and branch sway, which vary with sensor placement. In addition, at certain times of the day, the sensors were consistently shaded by opaque objects (top-crown from 15:30 to 17:00 LT in Fig. 1a) or consistently illuminated by the alignment of the sun and a forest clearing (mid-canopy from 11:00 to 12:00 LT in Fig. 1a).

The in-canopy horizontal heterogeneity in radiation is related to the forest canopy architecture. Old growth forests, such as the pristine tropical rainforest present at ATTO, are characterized by high rugosity which is defined as the standard deviation of the canopy height (Parker and Russ, 2004; Parker et al., 2019). The high forest rugosity is thought to relate with the horizontal variability in light transmissivity (Parker et al., 2019). Anhuf and Rollenbeck (2001) measured 36 vertical profiles of light transmissivity on a tropical rainforest. Their individual vertical profiles differed in the height and steepness where the largest light attenuation occurs. Comparing the individual vertical profiles with the average profile, it is noticeable that the individual profiles depict a more abrupt light attenuation than the average profile. This feature is also visible in our results, when we compare our individual PAR profile and the Beer–Lambert's (average) derived profile, Fig. 1b, c and d.

Because NEE and ET heavily depend on radiation, the not captured horizontal heterogeneity of radiation introduces uncertainty in our flux estimations. Because of that, modeled NEE and ET should be interpreted as indicative of a potential range of exchange across vertical layers, with the understanding that the underlying radiation measurements are highly local. We still regard our estimations valuable since they represent typical radiative perturbations that a single leaf experiences. However, in Appendix F, we provide a more conservative estimation of the ecosystem fluxes by using in-canopy radiation derived from Beer–Lambert's law (Fig. F.16), which results in ecosystem fluxes with smoother diurnal cycles (Figs. F.17 and F.18).

4.3. Modeled fluxes per layer

The transpiration and the net CO_2 assimilation was dominated by the top-crown layer (Fig. 7). Water use efficiency, calculated as the ratio between the CO_2 assimilated during daytime and the water transpired, increased with height (Table E.4), meaning that the CO_2 assimilation had greater vertical gradients than the transpiration. During nighttime, the understory respired less CO_2 than the mid-canopy and top-crown (Fig. 7a) likely because the understory leaves had to maintain less photosynthetic-related biochemical systems.

Despite producing reasonable results, the model may not fully capture some understory dynamics of the CO_2 exchange. The cumulative daytime CO_2 exchanged in the understory corresponded to a respiration of 1.92 g CO_2 m^{-2} (Table 2), indicating that those leaves were not being productive for the understory vegetation. Several factors could influence this outcome. Firstly, the understory PAR sensor may have been positioned in a particularly shaded area, potentially leading to an overestimation of the low light conditions in the 0–10 m layer. Secondly, the understory vegetation might exhibit greater photosynthetic activity under low light conditions than assumed in the model. Due to the lack of measured photosynthetic response curves to PAR, the same photosynthetic response to low light was applied across all canopy levels. However, understory vegetation often demonstrates higher tolerance to low light environments, being able to assimilate CO_2 at lower light intensities compared to mid-layer or top-crown vegetation (Sterck et al., 2013). Thirdly, the spectrum of light could also play a role in the understory CO_2 assimilation (Zhen et al., 2022; Jans et al., 2025; Wang et al., 2024). Within a forest, trees and plants primarily absorb radiation from the PAR wavelength (400–700 nm) and they transmit relatively enriched far-red light (700–750 nm). These far-red light can be used by plants for photosynthesis, particularly, when supplemented with radiation from the PAR wavelength spectrum (Zhen et al., 2022). The consideration of the far-red light for vegetation productivity is most important for shaded vegetation (Zhen et al., 2022) such as the understory represented in our study.

4.4. Ecosystem exchanges and the morning transition

Modeled and observed ecosystem fluxes (NEE and ET) showed strong agreement, exhibiting similar diurnal cycles and cumulative exchanges. This gives confidence on the ability of a three-layer model initialized by observations to reproduce forest fluxes. However, discrepancies were observed for NEE during the night and during some parts of the morning (from 7:30 to 9:00 LT), midday (from 10:30 to 12:00 LT) and afternoon (from 15:30 to 18 LT). During midday, the mid-canopy sensor measured persistent (local) illumination that probably overestimated the light condition of the layer, resulting in an overestimation of modeled NEE and ET. During the afternoon, modeled NEE could not be well studied due to a persistent (local) shade at the top-crown sensor. At night, discrepancies may stem from factors such as those identified by Aubinet et al. (2012), including the potential influence of advection terms, which may no longer be negligible.

During the morning, we observed differences particularly from 7:30 LT when the sensible heat flux became positive (Fig. C.13b) until 9 LT. This period is part of the morning transition. During the morning transition the nocturnal stable ABL shifts towards a well-mixed ABL. Convective turbulence during this phase entrains air from the nocturnal residual layer and free troposphere while flushing air stored within the canopy. These processes have been observed in Amazon rainforest studies (e.g., Culf et al., 1997; Araújo et al., 2002) and modeled by Dupont et al. (2024) (low wind case, Fig. 2c therein). The storage terms, which corrects observed turbulent fluxes to estimate ecosystem fluxes, played a different role for CO_2 and water. While the storage term for water (Fig. C.14b) had a minimal contribution to the total evapotranspiration, the storage term for CO_2 (Fig. C.14a) had a great impact on NEE during the morning. The magnitude and diurnal cycle of the CO_2 storage term align with prior estimates (Malhi et al., 1998; Araújo et al., 2002), peaking at approximate -10 μmol CO_2 m^{-2} s^{-1} in the morning and becoming smaller and positive in the afternoon. However, these estimates are subject to uncertainties, such as sampling limitations, where reducing the number of sensors can introduce a root mean square error of up to 20% (Xu et al., 2019).

Despite the inclusion of storage terms, modeled and observed NEE differed in the morning transition, particularly regarding the timing of the shift from net ecosystem respiration to net assimilation of CO_2. Previous studies (Malhi et al., 1998; Araújo et al., 2002) found that adding the storage term advanced this transition by 1–2 h. Similarly, Dupont et al. (2024) reported a 2-h anticipation for the top layer of their default canopy under low wind conditions (Fig. 9f). By contrast, in our study,

the inclusion only advanced the transition by 0.5 h. This mismatch underscores the complex dynamics of the morning transition, where flushing events, entrainment of air with varying CO_2 mixing ratios, and turbulence dependent on wind regimes all interact (Dupont et al., 2024).

5. Conclusions

In this research, we investigated the sub-diurnal variability of water and CO_2 fluxes across three canopy layers in a tropical rainforest during days characterized by shallow convection. We used and extended the continuous ATTO observational network during CloudRoots-Amazon22 field Camapign in the Amazonian dry season. These observations enable a detailed characterization of the microclimate (photosynthetic active radiation, temperature, vapor pressure deficit, CO_2 mixing ratios, wind and turbulence), leaf traits (maximum carboxylation rate, maximum electron transport and ^{13}C leaf isotopic composition), leaf gas exchange (stomatal conductance and sub-stomatal to atmospheric CO_2 mixing ratio), and above canopy ecosystem fluxes (turbulent fluxes and storage terms). The high temporal resolution of these observations allowed us to capture dynamic events, such as cloud-induced radiative perturbations and light penetration variability within the canopy. In this study, we first characterized the observed microclimate and leaf traits and then used the observed vertical profiles to drive a three-layer land-surface model which estimated ecosystem fluxes. The modeled ecosystem fluxes (NEE and ET) were then compared to fluxes observed above the canopy.

Our results revealed distinctive vertical profiles of microclimate and leaf traits that influenced the vegetation exchange of water and CO_2 and the air transport within the canopy. For instance, we observed a persistent daytime inversion of temperature within the canopy that hindered the air mixing between the mid-canopy and understory with the top-crown layer and the air aloft. In examining the contributions of different canopy layers to the ecosystem fluxes, we found that the top-crown layer played a dominant role in the diurnal patterns of NEE and ET. The mid-canopy layer contributed significantly to NEE and ET only when sufficient radiation penetrated the canopy, while the understory's contributions were generally modest. Overall, the modeled ecosystem fluxes, particularly ET, were in good agreement with those observed above the canopy. However, differences between observed and modeled NEE emerged at specific times: at night when CO_2 accumulated within the canopy, and during the morning transition (7:30 to 10:30 LT) when some of the accumulated CO_2 was released. These discrepancies underscore the importance of accurately representing CO_2 storage and release within the canopy, along with the associated ABL transient dynamics.

We believe that multi-layer canopy large-eddy simulations (LES) represent a powerful tool for investigating exchange dynamics across forest layers and for analyzing turbulent transport both above and within the canopy. LES offer high temporal resolution and effectively model the most energetic aspects of turbulence. Our findings emphasize the complexity of vertical gradients within forest canopies, including a variety of microclimatic variables, leaf traits, and canopy fluxes. These results provide a basis for comparison with multi-layer canopy LES and highlight the potential for future research incorporating vertical variability in forest microclimate and leaf traits.

CRediT authorship contribution statement

Raquel González-Armas: Writing – review & editing, Writing – original draft, Visualization, Validation, Supervision, Software, Project administration, Methodology, Investigation, Formal analysis, Data curation, Conceptualization. **Daniël Rikkers:** Writing – review & editing, Software, Methodology, Investigation, Formal analysis, Data curation. **Oscar Hartogensis:** Writing – review & editing, Supervision, Resources, Project administration, Conceptualization. **Cléo Quaresma Dias-Júnior:** Writing – review & editing, Resources, Data curation. **Shujiro Komiya:** Writing – review & editing, Resources, Data curation. **Giovanni Pugliese:** Writing – review & editing, Resources, Data curation. **Jonathan Williams:** Writing – review & editing, Resources, Data curation. **Hella van Asperen:** Writing – review & editing, Resources, Data curation. **Jordi Vilà-Guerau de Arellano:** Writing – review & editing, Writing – original draft, Visualization, Supervision, Resources, Project administration, Investigation, Funding acquisition, Conceptualization. **Hugo J. de Boer:** Writing – review & editing, Writing – original draft, Supervision, Resources, Project administration, Investigation, Data curation, Conceptualization.

Declaration of competing interest

The authors declare that they have no known competing financial interests or personal relationships that could have appeared to influence the work reported in this paper.

Acknowledgments

The CloudRoots-Amazon22 field campaign was part of the Cloudroots project (https://cloudroots.wur.nl/) and funded by Dutch Research Council (NWO; under the project Cloud-Roots - Clouds rooted in a heterogeneous biosphere with project number OCENW.KLEIN.407). The continuous measurements at ATTO were funded by the Bundesministerium für Bildung und Forschung, Germany (Contracts 01LB1001A, 01LK1602B, 01LK2101B), the Brazilian Ministério da Ciência, Tecnologia e Inovação (Contract 01.11.01248.00), the Max Planck Society, the Conselho Nacional de Desenvolvimento Científico e Tecnológico (CNPq, Brazil) (Process 200723/2015-4 and Grant 169842/2017-7), the FAPESP (Fundação de Amparo à Pesquisa do Estado de São Paulo) (Grant 2017/17047-0), and the CAPES project (Grant 88887.368025/2019-00). We acknowledge the support by the Instituto Nacional de Pesquisas da Amazônia, the Amazon State University, the Large-Scale Biosphere–Atmosphere Experiment, FAPEAM, the Reserva de Desenvolvimento Sustentável do Uatumã (SDS/CEUC/RDS337 Uatumã), and the Max Planck Society. We specially acknowledge everyone involved in the technical, logistic, and scientific support of the ATTO project such as the two professional tree climbers. We also extend our gratitude to David J. Fitzjarrald and the second anonymous reviewer, who have contributed to improving the quality of our manuscript and our research.

Appendix A. Radiation

A.1. Correlation between GHI and PAR above the canopy

To convert the clear sky global horizontal irradiance (GHI) reference to a clear sky PAR, a conversion factor was needed. To calculate it, we used observations from a spectroradiometer (FROST; Heusinkveld et al., 2023) located above the forest (at 63 m). This sensor measured different wavelengths and it was able to measure both GHI and PAR. The correlation between both quantities was high, Fig. A.9. By performing a linear regression with null intercept, we found the conversion equation: $PAR = 0.44 \cdot GHI$.

A.2. Radiative perturbations by clouds

During the selected days, shallow cumulus clouds were present. These clouds perturbed the incoming surface radiation by either casting shadows over the surface or by enhancing the incoming radiation due to scattering of nearby cloud edges. We classified the radiative effect of clouds in three categories: shade, no effect and enhancement, Fig. A.10. To identify the effect, we calculated the difference between the clear sky PAR reference and the value measured above the canopy. Whenever the difference was larger than 25 μmol m^{-2} s^{-1}, we identified it as

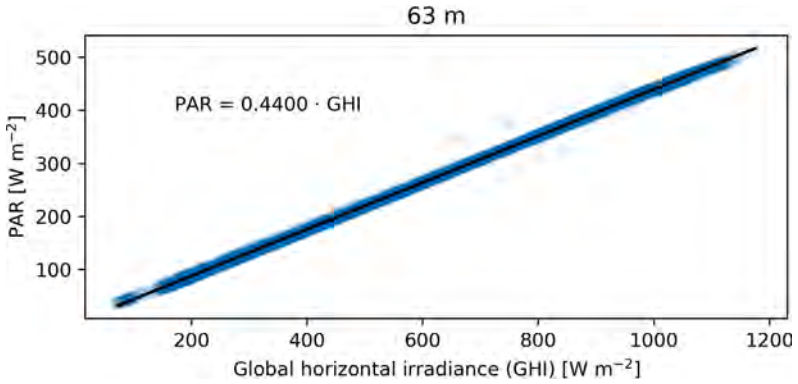

Fig. A.9. Scatterplot of observed PAR versus observed global horizontal irradiance between 7 and 17 LT. The radiation sensor was located at 63 m height. A linear fit with null intercept was performed to the observations to calculate a conversion factor between global solar irradiance and PAR.

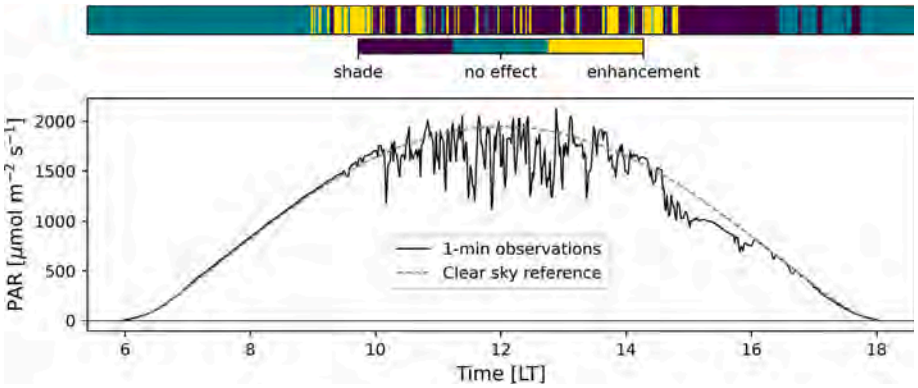

Fig. A.10. The bottom panel depicts time series of clear sky PAR reference (grey dashed line) and the observed above canopy PAR (black solid line). The upper panel indicates when the cloud is producing a shade (purple), an enhancement (yellow) or no effect (blue).

Table B.3
Mean observed A-g_s parameters for the three canopy layers.

Forest layer	$A_{mmax298}$ [μmol m^{-2} s^{-1}]	g_{m298} [mm s^{-1}]
Top-crown	17.6	2.63
Mid-canopy	11.9	2.25
Understory	6.8	1.46

a cloud enhancement. On the contrary, if the difference was smaller than −25 μmol m^{-2} s^{-1}, we identified it as cloud shade. If none of the previous conditions was met, we classified it as "no effect"."No effect" category can occur because there are not clouds or because they are not altering in a net manner the surface radiation.

Appendix B. Leaf traits

Photosynthesis response curves to sub-stomatal CO_2 concentration (Fig. B.11) were used to calculate parameters for the A-g_s leaf gas exchange model. The two calculated parameters were the maximum leaf photosynthetic capacity at 298 K ($A_{mmac298}$) and the mesophyll conductance at 298 K (g_{m298}). The fitted parameters can be found in Table B.3.

Appendix C. Observed ecosystem fluxes

Soil respiration was measured during CloudRoots-Amazon22 in ATTO. Mean soil respiration efflux had a mild diurnal cycle with values between 4.5 μmol CO_2 m^{-2} s^{-1} and 5 μmol CO_2 m^{-2} s^{-1}, Fig. C.12. Fig. C.13 shows time series of the friction velocity (u_*) and sensible heat flux (H). These two quantities enabled the determination of the morning transition, defined as the period when the sensible heat flux becomes positive until the time when the friction velocity stabilizes. Finally, in this section we show the time series of the storage fluxes of water and CO_2, Fig. C.14.

Appendix D. Up-scaling leaf fluxes to vegetation canopy fluxes

To calculate vegetation canopy fluxes from leaf fluxes, we need to account for the quantity of leaves that compose the canopy. We do so by integrating the leaf fluxes (leaf transpiration and leaf net CO_2 assimilation) over the cumulative leaf area index (L), Eq. (D.1). We assumed the vertical profile of leaf area density (LAD) and LAI (= 5.32 m^2 m^{-2}) reported by Gomes Alves et al. (2023) for ATTO site, Fig. D.15. The observations were carried out with a ground light detection and ranging sensor in October 2015 (details in Section 2.4 of Gomes Alves et al., 2023). The up-scaling from leaf fluxes to vegetation canopy fluxes was performed using the 3-point Gaussian quadrature method (Goudriaan, 1986). The Gaussian quadrature method was constructed to yield exact integration calculation for polynomials. In the case of the 3-point Gaussian quadrature, it is able to exactly integrate polynomials of degree 5 and lower. In the 3-point Gaussian quadrature, the function we aim to integrate, $f(L) = A_n(L)$ or $TR(L)$, is calculated as a weighted sum of the function evaluated at three points (L_1, L_2 and L_3), Eq. (D.2).

$$A_{n,canopy} = \int_0^{LAI} A_n(L)dL \quad ; \quad TR_{canopy} = \int_0^{LAI} TR(L)\,dL \tag{D.1}$$

$$\int_0^{LAI} f(L)dL \approx \frac{LAI}{3.6}\sum_{i=1}^{3} w_i \cdot f(L_i) \tag{D.2}$$

with weights: $w_1 = w_3 = 1$ and $w_2 = 1.6$, and points: $L_1 = (0.5 - \sqrt{0.15})LAI$, $L_2 = 0.5 \cdot LAI$ and $L_3 = (0.5 + \sqrt{0.15})LAI$

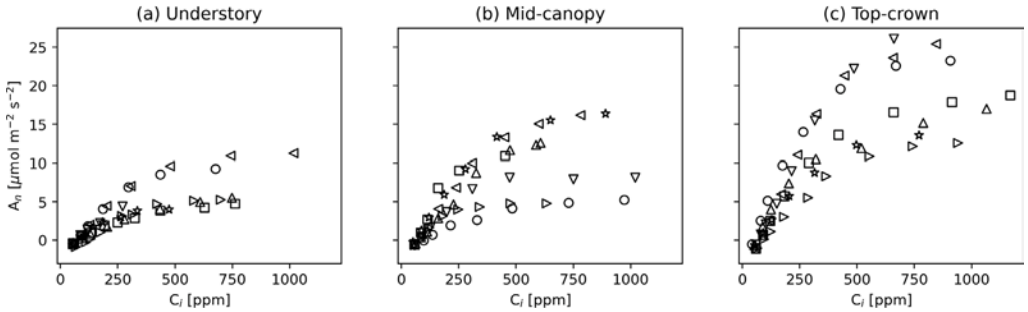

Fig. B.11. Measured A-C*i* response curves for the (a) understory, (b) mid-canopy and (c) top-crown forest layers. The symbols depict the individual curves, each performed in a different leaf.

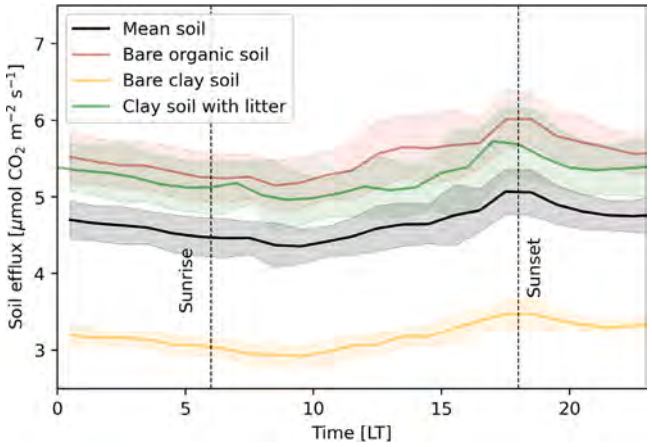

Fig. C.12. Time series of observed soil respiration efflux. The lines represent the measured soil respiration efflux for the 6-day composite in bare organic soil (red), bare clay soil (yellow), clay soil with litter (green), and the average of the three soil types (black). The shaded region indicates the range within one standard deviation of the mean and represents the variability across the individual days of the 6-day composite.

Given the assumed LAI and cumulative LAD profiles (Fig. D.15b), we can find the three heights where the functions ($A_n(L)$ and $TR(L)$) must be known. These quadrature heights are: 29.9 m for the top-crown, 18.9 m for the mid-canopy and 6.1 for the understory. These heights do not directly correspond with the heights where the sensors were positioned. In general, the sensors were located slightly lower (1–5 m) than the quadrature heights. We decided not to interpolate our observations over height to match the quadrature heights. Our reasoning was two-fold. First, a height interpolation would modify the measured temporal variability of the observed microclimate, maybe in ways that are not realistic, particularly for radiation. Second, the local canopy architecture surrounding the sensors may be different than that depicted by the mean LAD profile, introducing uncertainty to the quadrature heights estimation.

Finally, with the 3-point Gaussian quadrature approach, we decompose the ecosystem fluxes into the contributions of the understory, mid-canopy and top-crown. We do so by attributing $\frac{LAI}{3.6} w_1 \cdot f(L_1)$ to the top-crown, $\frac{LAI}{3.6} w_2 \cdot f(L_2)$ to the mid-canopy and $\frac{LAI}{3.6} w_3 \cdot f(L_3)$ to the understory.

Appendix E. Cumulative daytime NEE and ET (observations and modeled results)

To compare observed and model ecosystem fluxes, we calculated the cumulative daytime NEE and ET for both observations and model results, Table E.4. This quantity reflects the water and CO_2 exchanged per unit area from sunset until sunrise. To quantify the effect of the storage term, we also calculate the cumulative of the surface turbulent fluxes and compare it with the cumulative of the observed ecosystem fluxes which accounted for the storage.

Table E.4
Cumulative ecosystem water and CO_2 exchange per area during daytime. The table shows the cumulative for modeled NEE and ET, observed NEE and ET, and observed surface turbulent fluxes of water and CO_2 (F_{CO_2} and F_{H_2O}).

Variable	Units	Whole ecosystem (vegetation + soil)
$-\int_{sunrise}^{sunset} NEE_{modeled}\ dt$	g CO_2 m^{-2}	19.41
$-\int_{sunrise}^{sunset} NEE_{observed}\ dt$	g CO_2 m^{-2}	19.16
$-\int_{sunrise}^{sunset} F_{CO_2,observed}\ dt$	g CO_2 m^{-2}	16.03
$\int_{sunrise}^{sunset} ET_{modeled}\ dt$	kg H_2O m^{-2}	3.76
$\int_{sunrise}^{sunset} ET_{observed}\ dt$	kg H_2O m^{-2}	3.55
$\int_{sunrise}^{sunset} F_{H_2O,observed}\ dt$	kg H_2O m^{-2}	3.53

Appendix F. Calculation of the ecosystem fluxes with averaged in-canopy radiative fluctuations

Within the canopy, radiation measurements are sensitive to the position of the sensor. Because we used a PAR profile measured in a single tower, our leaf stomatal conductance (Fig. 6), canopy fluxes (Fig. 7) and ecosystem fluxes (Fig. 8) are sensitive to the local radiation fluctuations. Our estimated ecosystem fluxes (Figs. 7 and 8) represent the variability that an ecosystem would experience if subject to the strongly varying light environment that a leaf experiences.

As a sensitivity study, we have recalculated the fluxes using Beer–Lambert law estimations of radiation in the three layers (Fig. F.16). In doing so, we also eliminated the observed opaque shadow in the top-crown layer between 15:30 and 17:00 LT.

As expected, the resulting fluxes per layer have a smoother diurnal cycle (Fig. F.17) at all levels than when using the observed PAR profile (Fig. 7). In the mid-canopy and understory, the diurnal cycles of A_{nc} and TR are particularly symmetric around solar noon, indicating the maximum rates at midday. The modeled and observed ecosystem fluxes remain similar (Fig. F.18). The afternoon transition of the ecosystem from being a CO_2 sink into a source occurs at approximately 16:30 LT for both model and observations.

Data availability

Data will be made available on request.

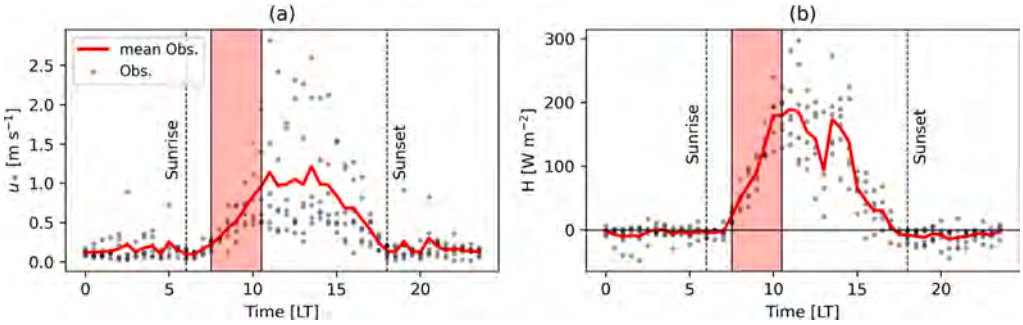

Fig. C.13. Time series of observed friction velocity (u_*) and sensible heat flux (H) at 50 m. Individual observations for the 6 shallow convective days are shown in grey points whereas the mean values are shown as a red line. H only accounts for the turbulent heat flux and it does not include a storage estimation. The red area indicates the morning transition defined to start when H becomes positive (7:30 LT) until when u_* stabilizes (10:30 LT).

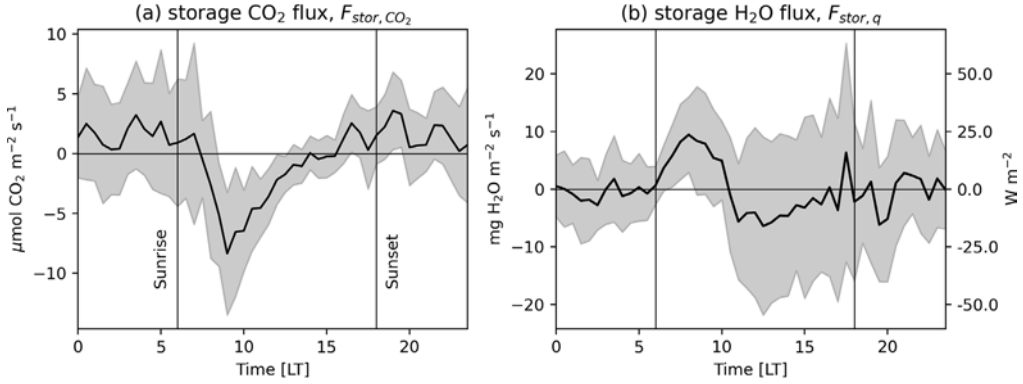

Fig. C.14. Time series of storage fluxes of (a) CO_2 and (b) water at 50 m. The solid line represents the mean value while the shaded region indicates the range within one standard deviation of the mean.

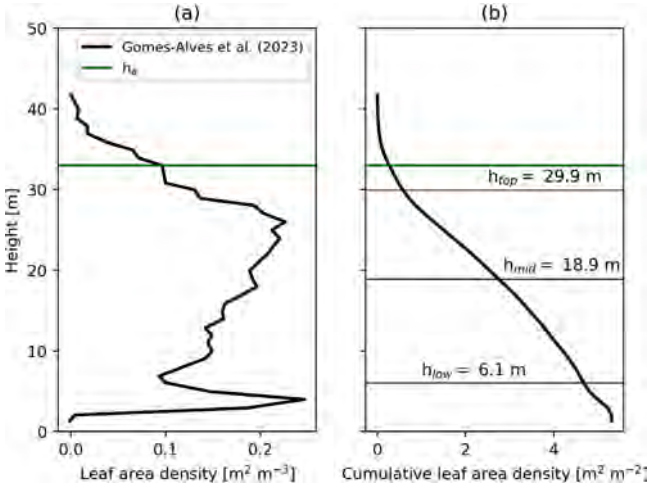

Fig. D.15. Leaf area density (a) and cumulative leaf area index (b) for terra firme upland rainforest. Values are based in Gomes Alves et al. (2023) study. The horizontal lines in panel (b) indicate the heights (h_{top}, h_{mid}, h_{low}) where the leaf fluxes are evaluated to up-scale to canopy fluxes using the 3-point Gaussian quadrature method.

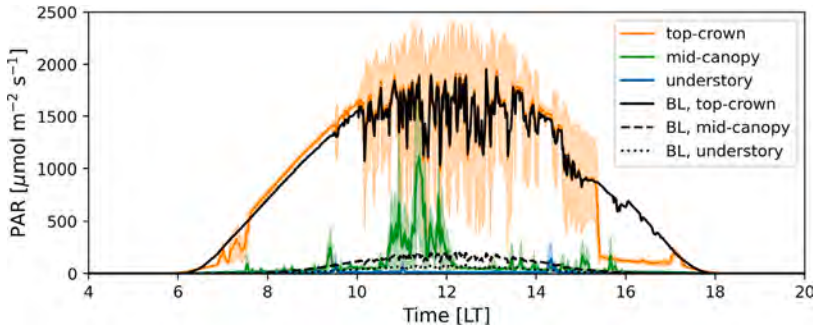

Fig. F.16. Time series of observed PAR as in Fig. 1 and Beer–Lambert's (BL) law estimation of PAR for the three canopy layers (shown in black lines).

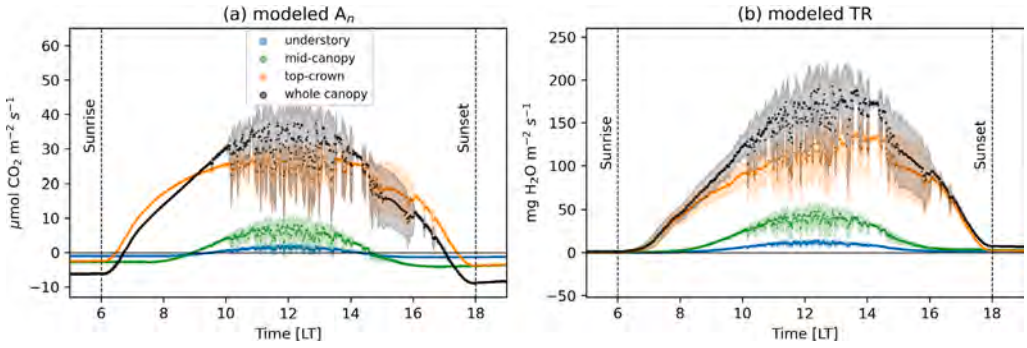

Fig. F.17. Same as Fig. 7 but for the model results using averaged in-canopy radiation.

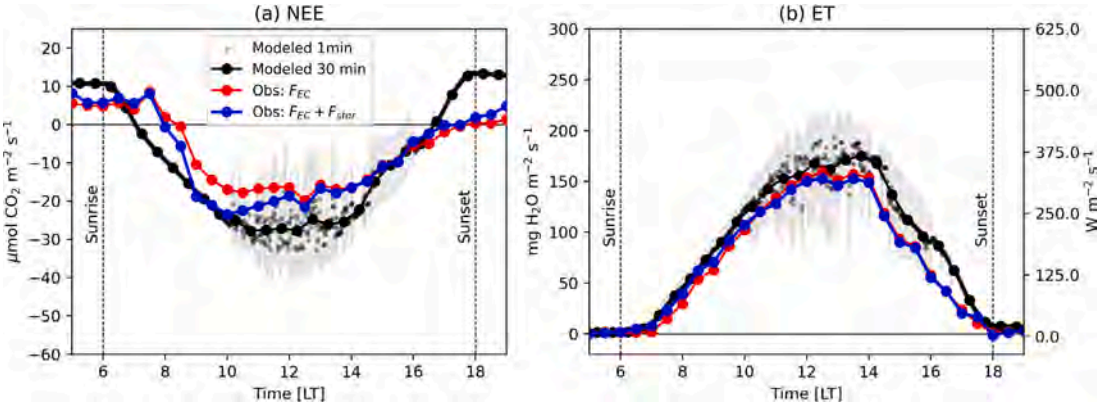

Fig. F.18. Same as Fig. 8 but for the model results using averaged in-canopy radiation.

References

Anav, A., Friedlingstein, P., Beer, C., Ciais, P., Harper, A., Jones, C., Murray-Tortarolo, G., Papale, D., Parazoo, N.C., Peylin, P., Piao, S., Sitch, S., Viovy, N., Wiltshire, A., Zhao, M., 2015. Spatiotemporal patterns of terrestrial gross primary production: A review. Rev. Geophys. 53 (3), 785–818. http://dx.doi.org/10.1002/2015RG000483.

Andreae, M.O., Acevedo, O.C., Araùjo, A., Artaxo, P., Barbosa, C.G.G., Barbosa, H.M.J., Brito, J., Carbone, S., Chi, X., Cintra, B.B.L., da Silva, N.F., Dias, N.L., Dias-Júnior, C.Q., Ditas, F., Ditz, R., Godoi, A.F.L., Godoi, R.H.M., Heimann, M., Hoffmann, T., Kesselmeier, J., Könemann, T., Krüger, M.L., Lavric, J.V., Manzi, A.O., Lopes, A.P., Martins, D.L., Mikhailov, E.F., Moran-Zuloaga, D., Nelson, B.W., Nölscher, A.C., Santos Nogueira, D., Piedade, M.T.F., Pöhlker, C., Pöschl, U., Quesada, C.A., Rizzo, L.V., Ro, C.-U., Ruckteschler, N., Sá, L.D.A., de Oliveira Sá, M., Sales, C.B., dos Santos, R.M.N., Saturno, J., Schöngart, J., Sörgel, M., de Souza, C.M., de Souza, R.A.F., Su, H., Targhetta, N., Tóta, J., Trebs, I., Trumbore, S., van Eijck, A., Walter, D., Wang, Z., Weber, B., Williams, J., Winderlich, J., Wittmann, F., Wolff, S., Yáñez Serrano, A.M., 2015. The Amazon tall tower observatory (ATTO): overview of pilot measurements on ecosystem ecology, meteorology, trace gases, and aerosols. Atmospheric Chem. Phys. 15 (18), 10723–10776. http://dx.doi.org/10.5194/acp-15-10723-2015.

Anhuf, D., Rollenbeck, R., 2001. Canopy structure of the Rio Surumoni rain forest (Venezuela) and its influence on microclimate. Ecotropica 7 (1–2), 21–32.

Araújo, A.C., Nobre, A.D., Kruijt, B., Elbers, J.A., Dallarosa, R., Stefani, P., von Randow, C., Manzi, A.O., Culf, A.D., Gash, J.H.C., Valentini, R., Kabat, P., 2002. Comparative measurements of carbon dioxide fluxes from two nearby towers in a central Amazonian rainforest: The Manaus LBA site. J. Geophys. Res.: Atmospheres 107 (D20), LBA 58–1–LBA 58–20. http://dx.doi.org/10.1029/2001JD000676.

Aubinet, M., Feigenwinter, C., Heinesch, B., Laffineur, Q., Papale, D., Reichstein, M., Rinne, J., Van Gorsel, E., 2012. Nighttime flux correction. In: Aubinet, M., Vesala, T., Papale, D. (Eds.), Eddy Covariance: A Practical Guide To Measurement and Data Analysis. Springer, pp. 133–157. http://dx.doi.org/10.1007/978-94-007-2351-1_5.

Belcher, S.E., Harman, I.N., Finnigan, J.J., 2012. The wind in the willows: Flows in forest canopies in complex terrain. Annu. Rev. Fluid Mech. 44, 479–504. http://dx.doi.org/10.1146/annurev-fluid-120710-101036.

Biosciences, L., 2019. Eddy covariance processing software (version 7.0. 6)[software].

Bonan, G.B., Patton, E.G., Finnigan, J.J., Baldocchi, D.D., Harman, I.N., 2021. Moving beyond the incorrect but useful paradigm: reevaluating big-leaf and multilayer plant canopies to model biosphere-atmosphere fluxes – a review. Agricult. Forest. Meterol. 306, 108435. http://dx.doi.org/10.1016/j.agrformet.2021.108435.

Botía, S., Gerbig, C., Marshall, J., Lavric, J.V., Walter, D., Pöhlker, C., Holanda, B., Fisch, G., de Araújo, A.C., Sá, M.O., Teixeira, P.R., Resende, A.F., Dias-Junior, C.Q., van Asperen, H., Oliveira, P.S., Stefanello, M., Acevedo, O.C., 2020. Understanding nighttime methane signals at the Amazon tall tower observatory (ATTO). Atmos. Chem. Phys. 20 (11), 6583–6606. http://dx.doi.org/10.5194/acp-20-6583-2020.

Carswell, F.E., Meir, P., Wandelli, E.V., Bonates, L.C.M., Kruijt, B., Barbosa, E.M., Nobre, A.D., Grace, J., Jarvis, P.G., 2000. Photosynthetic capacity in a central Amazonian rain forest. Tree Physiol. 20 (3), 179–186. http://dx.doi.org/10.1093/treephys/20.3.179.

Culf, A., Fisch, G., Malhi, Y., Nobre, C., 1997. The influence of the atmospheric boundary layer on carbon dioxide concentrations over a tropical forest. Agricult. Forest. Meterol. 85 (3), 149–158. http://dx.doi.org/10.1016/S0168-1923(96)02412-4.

Davidson, E.A., de Araújo, A.C., Artaxo, P., Balch, J.K., Brown, I.F., C. Bustamante, M.M., Coe, M.T., DeFries, R.S., Keller, M., Longo, M., Munger, J.W., Schroeder, W., Soares-Filho, B.S., Souza, C.M., Wofsy, S.C., 2012. The Amazon basin in transition. Nature 481 (7381), 321–328. http://dx.doi.org/10.1038/nature10717.

Dolman, A., Gash, J.H., Roberts, J., Shuttleworth, W., 1991. Stomatal and surface conductance of tropical rainforest. Agricult. Forest. Meterol. 54 (2), 303–318. http://dx.doi.org/10.1016/0168-1923(91)90011-E.

Dupont, S., Irvine, M.R., Bidot, C., 2024. Morning transition of the coupled vegetation canopy and atmospheric boundary layer turbulence according to the wind intensity. J. Atmos. Sci. http://dx.doi.org/10.1175/jas-d-23-0201.1.

Evans, J.R., Santiago, L.S., 2014. PrometheusWiki gold leaf protocol: gas exchange using LI-COR 6400. Funct. Plant Biol. 41 (3), 223–226. http://dx.doi.org/10.1071/FP10900.

Farquhar, G.D., von Caemmerer, S., Berry, J.A., 1980. A biochemical model of photosynthetic CO2 assimilation in leaves of C3 species. Planta 149 (1), 78–90. http://dx.doi.org/10.1007/BF00386231.

Farquhar, G.D., Ehleringer, J.R., Hubick, K.T., 1989. Carbon isotope discrimination and photosynthesis. Annu. Rev. Plant Biol. 40 (Volume 40, 1989), 503–537. http://dx.doi.org/10.1146/annurev.pp.40.060189.002443.

Farquhar, G., O'Leary, M., Berry, J., 1982. On the relationship between carbon isotope discrimination and the intercellular carbon dioxide concentration in leaves. Aust. J. Plant Physiol. 9, 121–137.

Finnigan, J.J., Shaw, R.H., Patton, E.G., 2009. Turbulence structure above a vegetation canopy. J. Fluid Mech. 637, 387–424. http://dx.doi.org/10.1017/S0022112009990589.

Fitzjarrald, D.R., Moore, K.E., Cabral, O.M.R., Scolar, J., Manzi, A.O., de Abreu Sá, L.D., 1990. Daytime turbulent exchange between the Amazon forest and the atmosphere. J. Geophys. Res.: Atmos. 95 (D10), 16825–16838. http://dx.doi.org/10.1029/JD095iD10p16825.

Foken, T., Leuning, R., Oncley, S., Mauder, M., Aubinet, M., 2012. Eddy covariance method. In: Aubinet, M., Vesala, T., Papale, D. (Eds.), Eddy Covariance: A Practical Guide to Measurement and Data Analysis. vol. 10, Springer, pp. 1–19. http://dx.doi.org/10.1007/978-94-007-2351-1.

Friedlingstein, P., Cox, P., Betts, R., Bopp, L., von Bloh, W., Brovkin, V., Cadule, P., Doney, S., Eby, M., Fung, I., Bala, G., John, J., Jones, C., Joos, F., Kato, T., Kawamiya, M., Knorr, W., Lindsay, K., Matthews, H.D., Raddatz, T., Rayner, P., Reick, C., Roeckner, E., Schnitzler, K.-G., Schnur, R., Strassmann, K., Weaver, A.J., Yoshikawa, C., Zeng, N., 2006. Results from the C4MIP model intercomparison. J. Clim. 19, 3337–3353. http://dx.doi.org/10.1175/JCLI3800.1.

Gentine, P., Green, J.K., Guérin, M., Humphrey, V., Seneviratne, S.I., Zhang, Y., Zhou, S., 2019. Coupling between the terrestrial carbon and water cycles—a review. Environ. Res. Lett. 14 (8), 083003. http://dx.doi.org/10.1088/1748-9326/ab22d6.

Giangrande, S.E., Feng, Z., Jensen, M.P., Comstock, J.M., Johnson, K.L., Toto, T., Wang, M., Burleyson, C., Bharadwaj, N., Mei, F., et al., 2017. Cloud characteristics, thermodynamic controls and radiative impacts during the observations and modeling of the green ocean Amazon (GoAmazon2014/5) experiment. Atmospheric Chem. Phys. 17 (23), 14519–14541.

Gomes Alves, E., Aquino Santana, R., Quaresma Dias-Júnior, C., Botía, S., Taylor, T., Yáñez Serrano, A.M., Kesselmeier, J., Bourtsoukidis, E., Williams, J., Lembo Silveira de Assis, P.I., Martins, G., de Souza, R., Duvoisin Júnior, S., Guenther, A., Gu, D., Tsokankunku, A., Sörgel, M., Nelson, B., Pinto, D., Komiya, S., Martins Rosa, D., Weber, B., Barbosa, C., Robin, M., Feeley, K.J., Duque, A., Londoño Lemos, V., Contreras, M.P., Idarraga, A., López, N., Husby, C., Jestrow, B., Cely Toro, I.M., 2023. Intra- and interannual changes in isoprene emission from central Amazonia. Atmos. Chem. Phys. 23 (14), 8149–8168. http://dx.doi.org/10.5194/acp-23-8149-2023, URL: https://acp.copernicus.org/articles/23/8149/2023/.

Goudriaan, J., 1986. A simple and fast numerical method for the computation of daily totals of crop photosynthesis. Agricult. Forest. Meterol. 38 (1), 249–254. http://dx.doi.org/10.1016/0168-1923(86)90063-8.

Goudriaan, J., Van Laar, H., Van Keulen, H., Louwerse, W., 1985. Photosynthesis, CO 2 and plant production. Wheat Growth Model. 107–122.

Grace, J., Lloyd, J., McIntyre, J., Miranda, A., Meir, P., Miranda, H., Moncrieff, J., Massheder, J., Wright, I., Gash, J., 1995. Fluxes of carbon dioxide and water vapour over an undisturbed tropical forest in south-west Amazonia. Global Change Biol. 1 (1), 1–12. http://dx.doi.org/10.1111/j.1365-2486.1995.tb00001.x.

Harrison, S.P., Cramer, W., Franklin, O., Prentice, I.C., Wang, H., Brännström, A., de Boer, H., Dieckmann, U., Joshi, J., Keenan, T.F., Lavergne, A., Manzoni, S., Mengoli, G., Morfopoulos, C., Peñuelas, J., Pietsch, S., Rebel, K.T., Ryu, Y., Smith, N.G., Stocker, B.D., Wright, I.J., 2021. Eco-evolutionary optimality as a means to improve vegetation and land-surface models. New Phytol. 231 (6), 2125–2141. http://dx.doi.org/10.1111/nph.17558.

Henkes, A., Fisch, G., Machado, L.A.T., Chaboureau, J.-P., 2021. Morning boundary layer conditions for shallow to deep convective cloud evolution during the dry season in the central Amazon. Atmospheric Chem. Phys. 21 (17), 13207–13225. http://dx.doi.org/10.5194/acp-21-13207-2021.

Heusinkveld, B.G., Mol, W.B., van Heerwaarden, C.C., 2023. A new accurate low-cost instrument for fast synchronized spatial measurements of light spectra. Atmos. Meas. Tech. 16 (15), 3767–3785. http://dx.doi.org/10.5194/amt-16-3767-2023.

Jacobs, C.M.J., 1994. Direct Impact of Atmospheric CO 2 Enrichment on Regional Transpiration. Wageningen University and Research.

Jans, T.B., Mossink, L., Wassenaar, M., Wientjes, E., Driever, S., Huber, M., Pierik, R., de Boer, H.J., 2025. Coupling modelling and experiments to analyse leaf photosynthesis under far-red light. Plant Cell Environ. 48 (5), 3171–3184. http://dx.doi.org/10.1111/pce.15340, https://onlinelibrary.wiley.com/doi/abs/10.1111/pce.15340, eprint: https://onlinelibrary.wiley.com/doi/pdf/10.1111/pce.15340.

Kruijt, B., Malhi, Y., Lloyd, J., Norbre, A.D., Miranda, A.C., Pereira, M.G.P., Culf, A., Grace, J., 2000. Turbulence statistics above and within two Amazon rain forest canopies. Bound.-Layer Meteorol. 94 (2), 297–331. http://dx.doi.org/10.1023/A:1002401829007.

Lefèvre, M., Schroedter-Homscheidt, M., Arola, A., 2019. Improving the McClear model estimating the downwelling solar radiation at ground level in cloud-free conditions – McClear-v3. Meteorol. Z. 28.

Lloyd, J., Grace, J., Miranda, A.C., Meir, P., Wong, S.C., Miranda, H.S., Wright, I.R., Gash, J.H.C., McIntyre, J., 1995. A simple calibrated model of Amazon rainforest productivity based on leaf biochemical properties. Plant Cell Environ. 18 (10), 1129–1145. http://dx.doi.org/10.1111/j.1365-3040.1995.tb00624.x.

Lloyd, J., Patiño, S., Paiva, R.Q., Nardoto, G.B., Quesada, C.A., Santos, A.J.B., Baker, T.R., Brand, W.A., Hilke, I., Gielmann, H., Raessler, M., Luizão, F.J., Martinelli, L.A., Mercado, L.M., 2010. Optimisation of photosynthetic carbon gain and within-canopy gradients of associated foliar traits for Amazon forest trees. Biogeosciences 7 (6), 1833–1859. http://dx.doi.org/10.5194/bg-7-1833-2010.

Malhi, Y., Nobre, A.D., Grace, J., Kruijt, B., Pereira, M.G.P., Culf, A., Scott, S., 1998. Carbon dioxide transfer over a central Amazonian rain forest. J. Geophys. Res.: Atmos. 103 (D24), 31593–31612. http://dx.doi.org/10.1029/98JD02647.

Parker, G.G., Fitzjarrald, D.R., Sampaio, I.C.G., 2019. Consequences of environmental heterogeneity for the photosynthetic light environment of a tropical forest. Agricult. Forest. Meterol. 278, 107661. http://dx.doi.org/10.1016/j.agrformet.2019.107661.

Parker, G.G., Russ, M.E., 2004. The canopy surface and stand development: assessing forest canopy structure and complexity with near-surface altimetry. Forest Ecol. Manag. 189 (1–3), 307–315. http://dx.doi.org/10.1016/j.foreco.2003.09.001.

Pugliese, G., Ingrisch, J., Meredith, L.K., Pfannerstill, E.Y., Klüpfel, T., Meeran, K., Byron, J., Purser, G., Gil-Loaiza, J., van Haren, J., Dontsova, K., Kreuzwieser, J., Ladd, S.N., Werner, C., Williams, J., 2023. Effects of drought and recovery on soil volatile organic compound fluxes in an experimental rainforest. Nat. Commun. 14 (1), 5064. http://dx.doi.org/10.1038/s41467-023-40661-8.

Raupach, M., Finnigan, J., 1988. Single-layer models of evaporation from plant canopies are incorrect but useful, whereas multilayer models are correct but useless': discuss. Aust. J. Plant Physiol. 15 (6), 705–716. http://dx.doi.org/10.1071/PP9880705, Cited by: 199.

Santana, R.A., Dias-Júnior, C.Q., da Silva, J.T., Fuentes, J.D., do Vale, R.S., Alves, E.G., dos Santos, R.M.N., Manzi, A.O., 2018. Air turbulence characteristics at multiple sites in and above the Amazon rainforest canopy. Agricult. Forest. Meterol. 260–261, 41–54. http://dx.doi.org/10.1016/j.agrformet.2018.05.027.

Santana, R.A.S.d., Dias-Júnior, C.Q., Vale, R.S.d., Tóta, J., Fitzjarrald, D.R., 2017. Observing and modeling the vertical wind profile at multiple sites in and above the Amazon rain forest canopy. Adv. Meteorol. 2017 (1), 5436157. http://dx.doi.org/10.1155/2017/5436157.

Seo, E., Dirmeyer, P.A., 2022. Understanding the diurnal cycle of land–atmosphere interactions from flux site observations. Hydrol. Earth Syst. Sci. 26 (20), 5411–5429. http://dx.doi.org/10.5194/hess-26-5411-2022.

Shuttleworth, W.J., 1984. Observations of radiation exchange above and below Amazonian forest. Q. J. R. Meteorol. Soc. 110 (466), 1163–1169. http://dx.doi.org/10.1002/qj.49711046623.

Shuttleworth, W.J., 1985. Daily variations of temperature and humidity within and above Amazonian forest. Weather 40 (4), 102–108. http://dx.doi.org/10.1002/j.1477-8696.1985.tb07489.x.

Shuttleworth, W.J., Leuning, R., Black, T.A., Grace, J., Jarvis, P.G., Roberts, J., Jones, H.G., Jarvis, P.G., Monteith, J.L., Shuttleworth, W.J., Unsworth, M.H., 1989. Micrometeorology of temperate and tropical forest. Philos. Trans. R. Soc. Lond. B, Biol. Sci. 324 (1223), 299–334. http://dx.doi.org/10.1098/rstb.1989.0050.

Sterck, F.J., Duursma, R.A., Pearcy, R.W., Valladares, F., Cieslak, M., Weemstra, M., 2013. Plasticity influencing the light compensation point offsets the specialization for light niches across shrub species in a tropical forest understorey. J. Ecol. 101 (4), 971–980. http://dx.doi.org/10.1111/1365-2745.12076.

Stocker, B.D., Wang, H., Smith, N.G., Harrison, S.P., Keenan, T.F., Sandoval, D., Davis, T., Prentice, I.C., 2020. P-model v1.0: an optimality-based light use efficiency model for simulating ecosystem gross primary production. Geosci. Model. Dev. 13 (3), 1545–1581. http://dx.doi.org/10.5194/gmd-13-1545-2020.

Sun, Y., Fu, R., Dickinson, R., Joiner, J., Frankenberg, C., Gu, L., Xia, Y., Fernando, N., 2015. Drought onset mechanisms revealed by satellite solar-induced chlorophyll fluorescence: Insights from two contrasting extreme events. J. Geophys. Res.: Biogeosci. 120 (11), 2427–2440. http://dx.doi.org/10.1002/2015JG003150.

Thomas, C., Foken, T., 2007. Organised motion in a tall spruce canopy: Temporal scales, structure spacing and terrain effects. Bound.-Layer Meteorol. 122 (1), 123–147. http://dx.doi.org/10.1007/s10546-006-9087-z.

van Diepen, K.H.H., Goudriaan, J., Vilà-Guerau de Arellano, J., de Boer, H.J., 2022. Comparison of C3 photosynthetic responses to light and CO2 predicted by the leaf photosynthesis models of Farquhar et al. (1980) and Goudriaan et al. (1985). J. Adv. Model. Earth Syst. 14 (9), e2021MS002976. http://dx.doi.org/10.1029/2021MS002976.

Vilà-Guerau de Arellano, J., Hartogensis, O., Benedict, I., de Boer, H., Bosman, P.J.M., Botía, S., Cecchini, M.A., Faassen, K.A.P., González-Armas, R., van Diepen, K., Heusinkveld, B.G., Janssens, M., Lobos-Roco, F., Luijkx, I.T., Machado, L.A.T., Mangan, M.R., Moene, A.F., Mol, W.B., van der Molen, M., Moonen, R., Ouwersloot, H.G., Park, S.-W., Pedruzo-Bagazgoitia, X., Röckmann, T., Adnew, G.A., Ronda, R., Sikma, M., Schulte, R., van Stratum, B.J.H., Veerman, M.A., van Zanten, M.C., van Heerwaarden, C.C., 2023. Advancing understanding of land–atmosphere interactions by breaking discipline and scale barriers. Ann. New York Acad. Sci. 1522 (1), 74–97. http://dx.doi.org/10.1111/nyas.14956.

Vilà-Guerau de Arellano, J., Hartogensis, O.K., de Boer, H., Moonen, R., González-Armas, R., Janssens, M., Adnew, G.A., Bonell-Fontás, D.J., Botía, S., Jones, S.P., van Asperen, H., Komiya, S., de Feiter, V.S., Rikkers, D., de Haas, S., Machado, L.A.T., Dias-Junior, C.Q., Giovanelli-Haytzmann, G., Valenti, W.I.D., Figueiredo, R.C., Farias, C.S., Hall, D.H., Mendonça, A.C.S., da Silva, F.A.G., da Silva, J.L.M., Souza, R., Martins, G., Miller, J.N., Mol, W.B., Heusinkveld, B., van Heerwaarden, C.C., D'Oliveira, F.A.F., Ferreira, R.R., Gotuzzo, R.A., Pugliese, G., Williams, J., Ringsdorf, A., Edtbauer, A., Quesada, C.A., Portela, B.T.T., Alves, E.G., Pöhlker, C., Trumbore, S., Lelieveld, J., Röckmann, T., 2024. CloudRoots-amazon22: Integrating clouds with photosynthesis by crossing scales. Bull. Am. Meteorol. Soc. http://dx.doi.org/10.1175/BAMS-D-23-0333.1.

Wang, Y., Braghiere, R.K., Yin, Y., Yao, Y., Hao, D., Frankenberg, C., 2024. Beyond the visible: Accounting for ultraviolet and far-red radiation in vegetation productivity and surface energy budgets. Glob. Chang. Biol. 30 (5), e17346. http://dx.doi.org/10.1111/gcb.17346.

Winderlich, J., Chen, H., Gerbig, C., Seifert, T., Kolle, O., Lavrič, J.V., Kaiser, C., Höfer, A., Heimann, M., 2010. Continuous low-maintenance CO_2/CH_4/H_2O measurements at the zotino tall tower observatory (ZOTTO) in central siberia. Atmos. Meas. Tech. 3 (4), 1113–1128. http://dx.doi.org/10.5194/amt-3-1113-2010.

Wofsy, S.C., Harriss, R.C., Kaplan, W.A., 1988. Carbon dioxide in the atmosphere over the Amazon basin. J. Geophys. Res.: Atmos. 93 (D2), 1377–1387. http://dx.doi.org/10.1029/JD093iD02p01377.

Xu, K., Pingintha-Durden, N., Luo, H., Durden, D., Sturtevant, C., Desai, A.R., Florian, C., Metzger, S., 2019. The eddy-covariance storage term in air: Consistent community resources improve flux measurement reliability. Agricult. Forest. Meterol. 279, 107734. http://dx.doi.org/10.1016/j.agrformet.2019.107734.

Zhen, S., van Iersel, M.W., Bugbee, B., 2022. Photosynthesis in sun and shade: the surprising importance of far-red photons. New Phytol. 236 (2), 538–546. http://dx.doi.org/10.1111/nph.18375.